

NORTHWESTERN UNIVERSITY

Computations of the Dynamic Fracture of Quasi-Brittle Plane and Shell
Structures by the Extended Finite Element Method

A DISSERTATION

SUBMITTED TO THE GRADUATE SCHOOL
IN PARTIAL FULFILLMENT OF THE REQUIREMENTS

for the degree

DOCTOR OF PHILOSOPHY

Field of Theoretical and Applied Mechanics

By

Jeong-Hoon Song

EVANSTON, ILLINOIS

June 2008

© Copyright by Jeong-Hoon Song 2008

All Rights Reserved

ABSTRACT

Computations of the Dynamic Fracture of Quasi-Brittle Plane and Shell Structures by
the Extended Finite Element Method

Jeong-Hoon Song

Finite element methods for the simulation of dynamic fracture in plane and thin shell structures and their application to quasi-brittle fracture problems are presented. The method is based on the extended finite element method (XFEM) and is incorporated within an explicit time integration scheme. The method is implemented using 4-node quadrilateral plane and Belytschko-Lin-Tsay shell elements, which have high computational efficiency because of their use of a one-point integration scheme. Discontinuities in the translational and angular velocity fields are introduced to model cracks by XFEM based on the Hansbo and Hansbo approach; the element which contains the crack is replaced by two superposed elements with additional phantom nodes. Though this discontinuity representation scheme uses the same linear combination of enrichment functions as the conventional XFEM, it allows for considerable simplifications in fractured plane and thin shell elements formalisms, and furthermore is applicable to arbitrary large deformations. Also, the method provides consistent history variables because it retains

the original quadrature points even for the integration of the discontinuous integrands of cracked elements.

When modeling fracture, the method employs a cohesive law with a fracture criterion. The development of a fracture criterion that is computationally efficient and is easily applied, in terms of available data, poses a significant difficulty. Fracture criteria for quasi-brittle materials are usually expressed in terms of the critical maximum principal tensile strain. However, in low order finite element models solved by explicit time integration, the maximum principal tensile strain tends to be quite noisy, so that crack paths computed by direct application of such criteria tend to be erratic and do not conform to experimentally observed crack paths. To circumvent these difficulties, a nonlocal form of a strain-based fracture criterion is developed. The nonlocal form is obtained by a kernel-weighted average over a sector in front of the crack tip.

The methodology is applied to the simulation of several experiments involving dynamic fracture and nonlinearities. They demonstrate that the method is able to reproduce the observed failure modes in the experiments quite well and they support the use of the developed methods for general applications of dynamic fracture.

Acknowledgements

I would like to express the deepest and sincerest gratitude to my advisor Professor Ted Belytschko. This thesis would not have come together without his support and guidance throughout my graduate studies. The last several years were an invaluable experience full of excitement and pleasure. I also would like to express my gratitude to Professor Professor Brian Moran and Leon M. Keer for serving on my Ph.D. committee, for their effort to review this work and for their helpful comments.

My decision to study computational mechanics and attend the Ph.D. program at Northwestern University was due primarily to my Masters advisor Professor Sang-Ho Lee, who was also Professor Ted Belytschko's graduate student. Now, as an Associate Dean of engineering school at Yonsei University in Korea, he continues to give me guidance towards my future career, for which I am grateful.

I would like to express thanks to my former and current collaborators: Dr. Areias, Dr. Loehnert, Dr. Rabczuk and Dr. Zi. Through collaborations on diverse research topics, I have been able to significantly extend my knowledge of computational mechanics. I would also like to thank the other people in the computational mechanics group at Northwestern University. Special thanks go to Robert Gracie, for many good discussions during coffee breaks, and to Mei Xu, who struggles with the parallelization of my codes.

I also thank my family for their unconditional support. Finally, I would like to express a great deal of sincere gratitude to my dear wife, Oh-Jung Kwon, for her warm support

and endless encouragement, which was essential for the success of this work and all things in my life.

Table of Contents

ABSTRACT	3
Acknowledgements	5
List of Figures	9
Chapter 1. Introduction	10
1.1. Objectives	10
1.2. Overview of finite element methods for dynamic fracture	11
1.3. Outline	19
Chapter 2. Phantom Node Method for Two Dimensional Plane Problems	21
2.1. Enriched displacement fields for discontinuity	22
2.2. Weak formulation and discretization	31
Chapter 3. Phantom Node Method for Shell Problems	37
3.1. Shell formulation with fracture	38
3.2. Element formulation	41
Chapter 4. Constitutive Models and Continuous-Discontinuous Transition	48
4.1. Constitutive models	49
4.2. Continuum to discontinuity transition	52
4.3. Cohesive crack models	54

Chapter 5. Numerical Examples	56
5.1. Dynamic fracture of two dimensional planes	56
5.2. Dynamic fracture of thin shells	70
Chapter 6. Conclusions	80
References	83
Vita	90

List of Figures

1.1	Nomenclature for a body which contains a discontinuity.	12
1.2	Representation of a crack by a set of deleted elements.	15
1.3	Schematic of the stress-strain curves for: (a) an elastic softening material and (b) a hardening plasticity material.	16
1.4	Schematic of: (a) a deleted element and (b) a linear elastic-linear softening material.	16
1.5	Schematic of the Xu and Needleman method [9] and (b) the Camacho and Ortiz method [10].	18
2.1	A two dimensional body with a discontinuity and its representation in the initial and the current domains.	22
2.2	A two dimensional discontinuity represented by two implicit functions $f(\mathbf{X})$ and $g(\mathbf{X}, t)$.	23
2.3	The representation of a discontinuity with an implicit functions $f(\mathbf{X})$ for the elementwise propagation of the discontinuity; the function $g(\mathbf{X}, t)$ is replaced by the set of gray elements.	23

2.4	A one dimensional representation of a discontinuity by: (a) the standard XFEM and (b) the phantom node method; solid and hollow circles denote the original nodes and the added phantom nodes, respectively.	24
2.5	The decomposition of a cracked two dimensional element with generic nodes 1 to 4 into two elements e_1 and e_2 ; solid and hollow circles denote the original nodes and the added phantom nodes, respectively.	28
2.6	The representation of a crack opening with the phantom node method; solid and hollow circles denote the original nodes and the added phantom nodes, respectively.	28
2.7	The decomposition of a shear element with generic nodes 1 to 4; dashed lines indicate phantom degrees of freedom.	31
2.8	Schematic of the conventional subdomain integration scheme for a cracked element.	34
2.9	Schematic of an one point integration scheme which can provide consistent history variables.	35
3.1	The nomenclature for a continuum shell.	39
3.2	Representation of a discontinuity in the reference configuration by a level set function $f(\boldsymbol{\xi})$ in the shell midsurface.	39
3.3	Nomenclature of a fractured shell: incompatible material overlapping may occur at the bottom surface due to the opening of the crack.	40

- 3.4 The decomposition of a cracked shell element with generic nodes 1–4 into two elements e_1 and e_2 ; solid and hollow circles denote the original nodes and the added phantom nodes, respectively. 43
- 3.5 Schematic of a crack opening in shell elements with the phantom node method; solid and hollow circles denote the original nodes and the added phantom nodes, respectively. 44
- 3.6 The decomposition of an element into three elements e_1 , e_2 and e_3 to model crack branching; solid and hollow circles denote the original nodes and the added phantom nodes, respectively. 45
- 4.1 Schematic of the averaging domain with a radius of r_c . 53
- 4.2 Schematic of a linear cohesive law: the area under the curve is the fracture energy, G_f . 55
- 5.1 Setup for the edge-cracked plate problem under impact loading: (a) the original experimental setup and (b) its numerical model. 57
- 5.2 The crack path for a 100×100 quadrilateral mesh with a Lemaitre damage model at different time steps: (a) $t = 39.29 \mu\text{s}$, (b) $t = 42.86 \mu\text{s}$, (c) $t = 53.58 \mu\text{s}$ and (d) $t = 88.58 \mu\text{s}$. 59
- 5.3 Comparison of the crack paths for a 50×50 and a 100×100 quadrilateral meshes with a Lemaitre damage model at $t = 88.58 \mu\text{s}$: (a) a 50×50 quadrilateral mesh and (b) a 100×100 quadrilateral mesh. 59
- 5.4 Crack propagation speed for the edge-cracked plate problem under impulsive loading: (a) the current method and (b) the previous results

- in Reference [11]; in Reference [11] a 80×80 cross-triangular mesh was used. 60
- 5.5 Crack paths for the element deletion method with: (a) a 100×100 structured quadrilateral mesh at $t = 60.19 \mu s$ and (b) an unstructured mesh ($h_{avg}^e = 1.0 \text{ mm}$) at $t = 67.85 \mu s$. 61
- 5.6 The crack paths of the interelement crack method of Xu and Needleman [9] with 50×50 and 100×100 quadrilateral meshes: (a) $t = 98.65 \mu s$ and (b) $t = 98.73 \mu s$. 61
- 5.7 The crack paths of the simulations with the damage model and the elasto-viscoplastic model. 63
- 5.8 Dynamic shear band propagation: (a) effective plastic strain distribution at $t = 35.00 \mu s$ and (b) comparison of the computed shear band path with experimental results [56]. 63
- 5.9 Plate with a horizontal initial notch under tensile loading. 64
- 5.10 Crack branching and damage evolution with a 100×51 mesh at different time steps: (a) $t = 30.29 \mu s$ (b) $t = 46.14 \mu s$ (c) $t = 55.93 \mu s$ and (d) a sketch of the experiment paths reported by Ramulu and Kobayashi [62]. 65
- 5.11 Crack propagation speed for the crack branching problem: (a) the current method and (b) the previous results in Reference [11]. 66
- 5.12 The final crack path of the element deletion method with a 200×81 structured quadrilateral mesh at different time steps: (a) $t = 30.56 \mu s$ and (b) $t = 65.62 \mu s$. 66

- 5.13 Crack propagation speed for the crack branching problem: (a) the element deletion method and (b) Camacho and Ortiz method [10]. 67
- 5.14 Crack path of the Camacho and Ortiz method [10] with: a 76×30 structured cross-triangular mesh at (a) $t = 48.38 \mu s$; (b) $t = 100.00 \mu s$ and a 152×60 structured cross-triangular mesh at (c) $t = 48.09 \mu s$; (d) $t = 100.0 \mu s$. The deformed shapes are magnified by 90. 68
- 5.15 The final crack paths for unstructured meshes ($h_{avg}^e = 1.0 \text{ mm}$): (a) the element deletion method and (b) the Camacho and Ortiz method [10]; the deformed shapes are magnified by 90. 69
- 5.16 Setup for the notched cylinder fracture test under internal detonation pressure [67, 68]: (a) the total experiment assembly, (b) the cylinder with the notch size of $L = 5.08 \text{ cm}$ (*shot7*) and (c) the cylinder with a notch size of $L = 2.54 \text{ cm}$ (*shot4*). 71
- 5.17 Evolution of the crack paths and the distributions of effective plastic stress for the cylinder with the notch size of $L = 5.08 \text{ cm}$ (*shot7*) at different time steps: (a) $t = 213.55 \mu s$, (b) $t = 228.61 \mu s$, and (c) $t = 238.01 \mu s$. Note that the finite element nodes are plotted and the crack paths are explicitly marked. 74
- 5.18 Crack opening at time $t = 256.86 \mu s$ along with the distribution of effective plastic stress for the cylinder with the notch size of $L = 5.08 \text{ cm}$ (*shot7*): (a) side view, and (b) top view. Note that the finite element nodes are plotted and the crack paths are explicitly marked. 75

- 5.19 Comparison of the final deformed shape for the cylinder with the notch size of $L = 5.08$ cm (*shot7*): (a) the simulation result, and (b) the experimental result [67, 68]. 75
- 5.20 Propagation speeds of two crack tips for the cylinder with the notch size of $L = 5.08$ cm (*shot7*). 76
- 5.21 Evolution of the crack and the distributions of the effective plastic stress for the cylinder with the notch size of $L = 2.54$ cm (*shot4*) at different time steps: (a) $t = 231.41 \mu\text{s}$ and (b) $t = 239.05 \mu\text{s}$. Note that the finite element nodes are plotted and the crack paths are explicitly marked. 77
- 5.22 Crack propagation speeds of two crack tips for the cylinder with the notch size of $L = 2.54$ cm (*shot4*). 77
- 5.23 Evolution of the crack paths and the distributions of the effective plastic stress for the cylinder with the notch size of $L = 2.54$ cm (*shot4*) at time $t = 261.98 \mu\text{s}$: (a) top view and (b) side view. Note that the finite element nodes are plotted and the crack paths are explicitly marked. 78
- 5.24 Comparison of the final deformed shape for the cylinder with the notch size of $L = 2.54$ cm (*shot4*) at time $t = 298.1 \mu\text{s}$: (a) the simulation result, and (b) the experimental result (*shot 4*). 79

CHAPTER 1

Introduction

This chapter provides an introduction to various finite element methods for dynamic fracture. Section 1.1 gives the objectives of the thesis. The following section reviews some of the previous work on finite element methods for dynamic fracture. Finally, section 1.3 presents an outline of the remainder of the thesis.

1.1. Objectives

The main objective of this work is to develop a numerical scheme for modeling quasi-brittle dynamic fracture by means of the extended finite element method (XFEM) [1, 2]. The methodology is intended primarily for shells, but some of the preliminary work was done in the context of two dimensional plane problems. The following goals have been identified to meet our primary objective:

- (1) Develop an efficient and accurate formulation for dynamic fracture based on the XFEM basis functions.
- (2) Develop a fracture criterion that is computationally efficient and is easily applied within the framework of explicit dynamic methods.
- (3) Demonstrate the effectiveness and robustness of the proposed method with numerical examples for dynamic crack propagation with two dimensional plane and shell structures.

1.2. Overview of finite element methods for dynamic fracture

The finite element method is one of the most popular numerical methods in solid mechanics due to its robustness. A classical way for modeling discontinuities such as cracks and shear bands in finite elements is to model them coincident with element edges and then introduce an additional set of nodes so that the interpolation functions across the element edge can be discontinuous; for growing cracks, these are called remeshing methods. In this approach, when the discrete equations are developed from a Galerkin weak form, the correct interface condition are provided naturally. Examples are Ingraffea *et al.* [3], Swenson and Ingraffea [4, 5], Bittencourt *et al.* [6], Martha *et al.* [7], and Neto *et al.* [8].

However, these remeshing methods [3, 4, 5, 6, 7, 8] are quite unwieldy for modeling evolving discontinuities because they require mesh generation in each time step and projections of field variables from the previous time step. Furthermore, even with excellent projection schemes, significant errors can be introduced in the velocities, stresses and displacements by projection. Also, in most dynamic crack propagation problems, the crack advances over a large part of the mesh, so that remeshing would need to be performed many times. Even for modeling of the stationary discontinuities, these methods can be quite cumbersome, because the construction of a mesh that conforms the element edges and the cracks surfaces is often awkward for mesh generation.

To circumvent these difficulties, several different types of numerical methods for modeling dynamic crack growth have been proposed. We cannot review the entire literature here, but summarize some of the key works on the major methods. In the following sections, we reviews the key works with emphasis on:

- (1) the extended finite element method [1, 2]
- (2) the element deletion method
- (3) the interelement crack method [9, 10]

1.2.1. Review of the extended finite element method

The extended finite element method (XFEM) [1, 2] was first applied to two dimensional dynamic fracture problems in Belytschko *et al.* [11] and has since been developed for two dimensional multiple crack growth [12, 13], two dimensional dynamic fracture problems [11, 14], three dimensional static crack propagation problems [15], and recently for dynamic fracture of shells [16, 17, 18].

One of the underlying key concepts in the XFEM is the partition of unity [19, 20]. In the partition of unity approach, the approximation basis is spanned by the standard finite element approximation space and extended by the products of the standard finite element shape functions with special local characteristic functions which are constructed from knowledge about the solution.

To describe these concepts in more detail, consider a domain Ω which contains a discontinuity Γ_c , as shown in Figure 1.1. In the classical partition of unity method [19, 20],

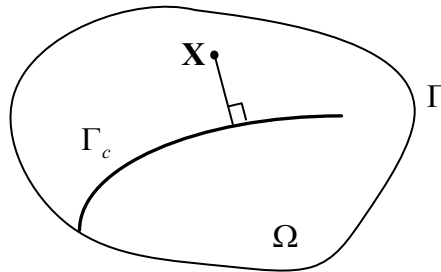


Figure 1.1. Nomenclature for a body which contains a discontinuity.

the domain Ω is divided into subdomains Ω_I and then a set of unity functions \mathcal{N}_I is selected so that the supports of \mathcal{N}_I corresponds to Ω_I and furthermore

$$\sum_I \mathcal{N}_I = 1 \text{ in } \Omega \quad (1.1)$$

A local characteristic of the solution can then be incorporated into the approximation by letting

$$\mathbf{u}^{loc}(\mathbf{X}) = \sum_I \mathcal{N}_I(\mathbf{X}) \Psi(\mathbf{X}) \mathbf{q}_I \quad (1.2)$$

where \mathbf{q}_I are arbitrary parameters that are obtained as part of the solution process and the function $\Psi(\mathbf{X})$, often called *an enrichment function*, since its product with the partition of unity functions \mathcal{N}_I enriches the approximation space. The partition of unity functions, \mathcal{N}_I , can be the standard finite element shape functions with domain corresponding to the elements surround node I . Note that Equation (1.2) implies that the classical partition of unity method [19, 20] applies the enrichment to the entire domain and so would entail considerable computational expense.

However, in the XFEM a *local partition of unity* with a discontinuous enrichment that only spans one element and vanishes at the edges is constructed instead of a global partition of unity. In this approach, the partition of unity is only applied locally in a subdomain around the feature that requires enrichment: i.e. for fracture problems, a discontinuous function that only spans the elements that contain the crack, and vanishes at the edges of these elements is used. In this case, Equation 1.2 can be written as

$$\mathbf{u}^{loc}(\mathbf{X}) = \sum_{I \in \mathcal{S}_c} \mathcal{N}_I(\mathbf{X}) \Psi(\mathbf{X}) \mathbf{q}_I \quad (1.3)$$

where N_I is a conventional finite element shape function and \mathcal{S}_c is the set of locally enriched nodes.

In a fracture problem, the displacement field is decomposed into a continuous and discontinuous parts since the major local characteristic behavior is the discontinuity in displacement field:

$$\mathbf{u}^h(\mathbf{X}, t) = \mathbf{u}^{cont}(\mathbf{X}, t) + \mathbf{u}^{disc}(\mathbf{X}, t) \quad (1.4)$$

where \mathbf{u}^{cont} and \mathbf{u}^{disc} denote continuous and discontinuous parts of the solutions at material points \mathbf{X} and time t , respectively. Note that in the above decomposition, the continuous part of the solution is the standard finite element field, whereas the discontinuous part of the solution is the enriched field. The approximation of the conventional XFEM displacement field is given by

$$\mathbf{u}^h(\mathbf{X}, t) = \sum_I N_I(\mathbf{X}) \{ \mathbf{u}_I(t) + H(f(\mathbf{X})) \mathbf{q}_I \} \quad (1.5)$$

where \mathbf{u}_I and \mathbf{q}_I are the regular and enrichment nodal variables, respectively, and $H(\cdot)$ is the Heaviside step function given by

$$H(x) = \begin{cases} 1 & x > 0 \\ 0 & x \leq 0 \end{cases} \quad (1.6)$$

and $f(\mathbf{X})$ is the level set function used to define the location of the discontinuity: see Stolarska *et al.* [21], Belytschko *et al.* [22], Ventura *et al.* [23, 24], and Prabel *et al.* [25]. In XFEM, the enrichment is injected when a criterion for crack nucleation or crack growth is met.

1.2.2. Review of the element deletion method

The element deletion method, often called element erosion, is the one of the simplest methods which can simulate fracture problems within the framework of the conventional FEM without complicated modifications. The attractiveness of the method lies in the fact that it requires no alteration of standard finite element software. One can simply introduce a discontinuity with constitutive equations in which the stress vanishes at specified criteria or due to a damage law. Because of their simplicity, these methods have been widely used in industry.

More precisely, a set of deleted elements which have zero stress, i.e. zero material resistance, is used to model a crack as shown in Figure 1.2. This is implemented by constitutive equations in which the stress tends to zero for sufficiently large strain; examples of such stress-strain laws are shown in Figure 1.3.

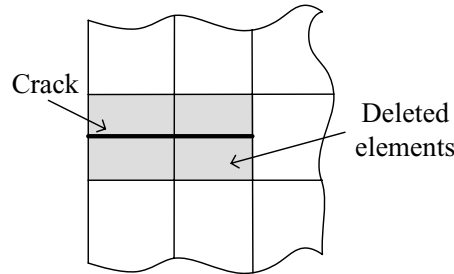


Figure 1.2. Representation of a crack by a set of deleted elements.

One of the crucial points in using the element deletion method is the scaling of the constitutive equation. In the element deletion method, it is imperative that the constitutive equation be adjusted with respect to the element size so that the fracture energy is independent of element size. Unless the constitutive equation is adjusted to reflect element size, the energy released due to deleting an element depends on the element size,

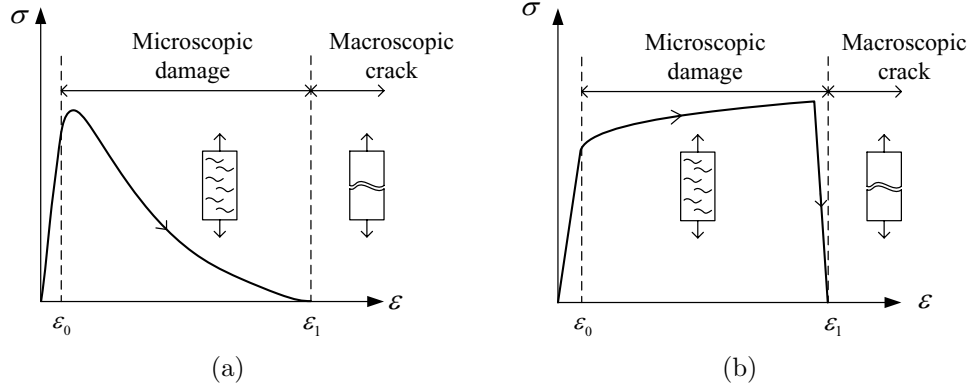


Figure 1.3. Schematic of the stress-strain curves for: (a) an elastic softening material and (b) a hardening plasticity material.

which causes spurious mesh dependency. However, even with these modifications in the constitutive equations, the element deletion method suffers from substantial mesh dependence; in Song *et al.* [26], it was shown that the element deletion method completely fails in the prediction of crack branching for structured meshes.

Consider a linear elastic-linear softening constitutive model as shown in Figure 1.4(b). In the application of the element deletion method, the energy dissipation in an element

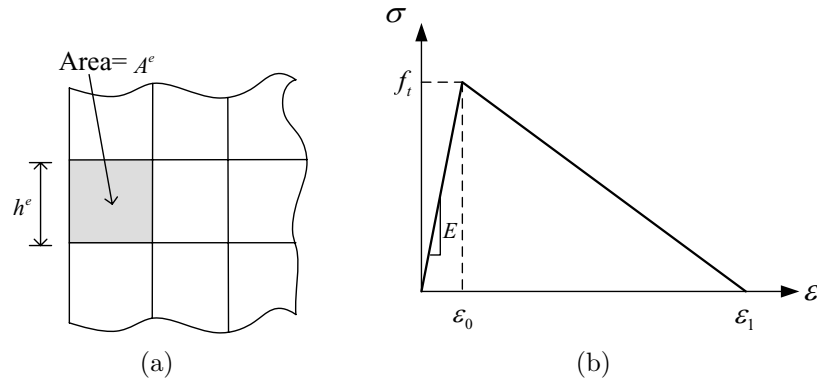


Figure 1.4. Schematic of: (a) a deleted element and (b) a linear elastic-linear softening material.

with this stress-strain law is then equated to the surface energy of a crack passing through the element parallel to the element sides by modifying the stress strain law. This energy consistency renders solutions relatively mesh size independent. Generally, no information about the orientation of the crack surface is included, so it is best to use square or nearly square elements. To obtain energy equivalence in two dimensional problems for the stress-strain law shown in Figure 1.4, the upper strain limit ϵ_1 is scaled so that

$$G_f h^e = \frac{1}{2} E \epsilon_0 \epsilon_1 A^e \quad (1.7)$$

where G_f is the fracture energy, h^e is a characteristic dimension (the length of a side for a square element), and A^e is the area of the element (unit thickness is assumed).

1.2.3. Review of the interelement crack method

The interelement crack method employs discontinuity models that are identical to those in remeshing methods; i.e. element edges coincident with the discontinuity modeled with independent nodes on opposite sides. No effort is needed to track the discontinuity with remeshing, but these methods rely on dense meshes to approximately capture the topology of the discontinuity and on cohesive surfaces to model the nucleation and evolution of the discontinuity. Two forms have evolved: methods where element edge separation is possible on all edges from the beginning of the simulation as in Xu and Needleman [9] and methods where the cohesive surfaces is injected selectively, as developed by Camacho and Ortiz [10], and Ortiz and Pandolfi [27]; see Figure 1.5. In the former, some errors are introduced in the bulk properties of the material and convergence is not clear. Papoulia *et al.* [28, 29] have also pointed out that errors occur due to lack of continuity in injected

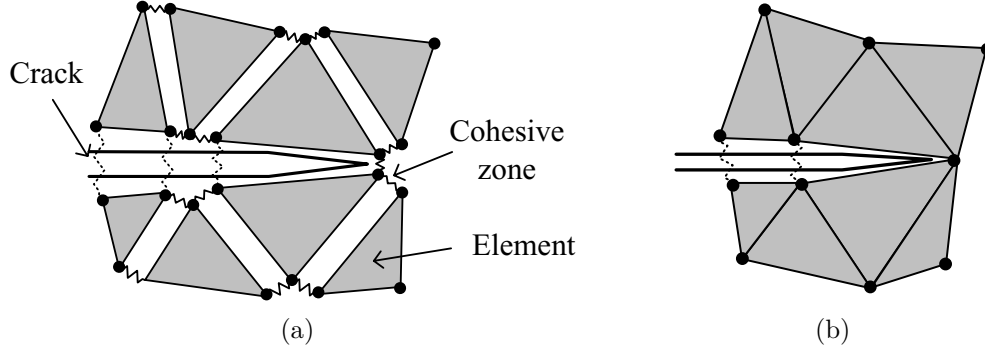


Figure 1.5. Schematic of the Xu and Needleman method [9] and (b) the Camacho and Ortiz method [10].

cohesive laws; these must also be considered in the use of XFEM with cohesive traction laws on the faces formed by cracks. Overall, these methods show a significant degree of mesh sensitivity [11, 26], although Zhou and Molinari [30] have shown that introducing a degree of randomness in the cohesive strength ameliorates this problem.

In the Xu and Needleman [9] approach, all of element edges are mechanically joined from the beginning of the simulation by cohesive laws of the form:

$$T_n = -\frac{\phi_n}{\Delta_n} e^{(-\delta_n/\Delta_n)} \left\{ \frac{\delta_n}{\Delta_n} e^{(-\delta_n^2/\Delta_n^2)} + \frac{1-q}{r-1} [1 - e^{(-\delta_n^2/\Delta_n^2)}] \left(r - \frac{\delta_n}{\Delta_n} \right) \right\} \quad (1.8)$$

$$T_t = -\frac{\phi_n}{\Delta_n} \left(2 \frac{\Delta_n}{\Delta_t} \right) \frac{\delta_t}{\Delta_t} \left\{ q + \frac{r-q}{r-1} \frac{\delta_n}{\Delta_n} \right\} e^{(-\delta_n/\Delta_n)} e^{(-\delta_t^2/\Delta_t^2)} \quad (1.9)$$

where \mathbf{T} is the traction across the interelement surface, subscripts n and t denote the normal and tangential components, respectively, δ is the displacement jump across the cohesive surface interface, ϕ is the cohesive potential function, and Δ is a characteristic length; for details, refer to [9]. In the Camacho and Ortiz approach [10], elements are allowed to separate along edges only when a fracture criterion is met or the element edges

are contiguous to a crack tip: the criterion is given by

$$\sigma^{eff} = \sqrt{\sigma_n^2 + \beta^{-2}\sigma_t^2} \geq \sigma_{fr} \quad (1.10)$$

where σ_n and σ_t are the normal and tangential stress along an element edge, respectively, and σ_{fr} is the material fracture strength. The cohesive law used in Camacho and Ortiz [10] is

$$T_n = e \frac{\sigma_c}{\delta_c} \beta^2 \delta_s e^{-\delta/\delta_c} \quad (1.11)$$

$$T_t = e \frac{\sigma_c}{\delta_c} \delta_n e^{-\delta/\delta_c} \quad (1.12)$$

where σ_c and δ_c are the maximum cohesive traction and critical opening displacement, respectively; for details, refer to [10]. Once a criterion for insertion of the cohesive law is met, the crack automatically chooses its path by solving the momentum equation that takes into account the traction forces on the cohesive edges. The method is further developed in Ortiz and Pandolfi [27].

1.3. Outline

The remainder of this thesis is as follows: in Chapter 2, a new formulation for the modeling of discontinuities in two dimensional plane problems that is particularly suited to explicit time integration methods is presented and then, in Chapter 3, the proposed method is extended for shells. Chapter 4 reviews some of constitutive models which are used in this work along with a cohesive model and fracture criteria. In Chapter 5, numerical examples for finite strain elastic and elasto-plastic crack propagation are

provided to demonstrate the effectiveness and the robustness of the method. Finally, Chapter 6 presents the conclusions.

CHAPTER 2

Phantom Node Method for Two Dimensional Plane Problems

We present a method for the modeling of dynamic crack propagation for two dimensional plane problems that is particularly suited to explicit time integration methods. The formulation enables crack propagation to be easily treated by low order elements, particularly with one-point quadrature elements; it is also applicable to shear bands. The method is based on the XFEM [11], but it uses a transformation of the nodal variables that leads to the superposed element formalism of Hansbo and Hansbo [31].

The advantage of this formalism is that an element containing a discontinuity is replaced by two elements with additional phantom nodes or phantom degrees of freedom, so that little modification of existing explicit finite element programs is needed to implement this formulation for elements with cracks or shear bands. The associated shape functions in a cracked or sheared element are identical to the shape functions of an intact element, which leads to certain simplifications of the implementation in existing codes. Within this context, we have also developed simple quadrature rules for the elements with cracks and shear bands that involve only a single quadrature point for each of the superposed elements.

In the description of a crack, we use implicit functions, i.e. level set functions, to describe the geometry of the cracks, as proposed in Stolarska *et al.* [21] and Belytschko *et al.* [22]. This is not an intrinsic part of the approach, although it does simplify implementations, particularly in three dimensions, which are not considered here.

2.1. Enriched displacement fields for discontinuity

Consider an initial domain $\Omega_0 \in \mathcal{R}^2$, as shown in Figure 2.1. The motion is described by $\mathbf{x} = \phi(\mathbf{X}, t)$, where \mathbf{X} and \mathbf{x} denote material and spatial coordinates, respectively. In the current domain, the image of the initial domain Ω_0 is denoted by Ω . We allow this domain to contain an internal discontinuity Γ_c which is enveloped by a region Ω_c . Inside of the region Ω_c , we defined two local functions $f(\mathbf{X})$ and $g(\mathbf{X}, t)$ where $f(\mathbf{X})$ and $g(\mathbf{X}, t)$ are the signed distance function that describe the crack surface and tip geometry, respectively. The surface $f(\mathbf{X}) = 0$ corresponds to the crack surface denoted by Γ_c and the function $g(\mathbf{X}, t)$ is defined so that $g(\mathbf{X}, t) > 0$ along the crack surface and vanishes at the crack tip as shown in Figure 2.2.

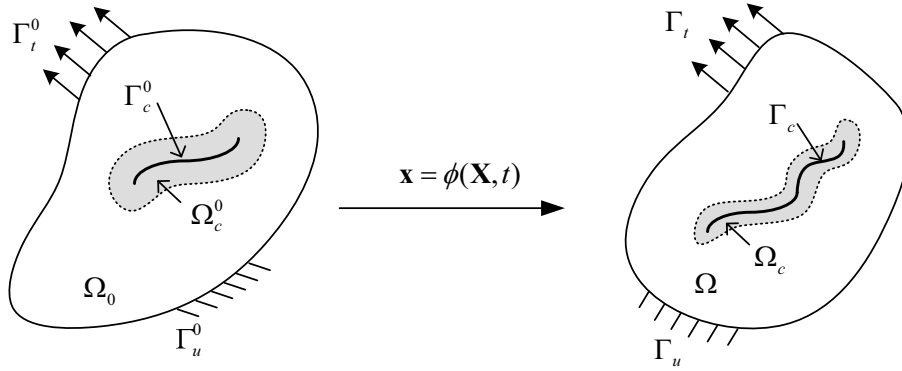


Figure 2.1. A two dimensional body with a discontinuity and its representation in the initial and the current domains.

The crack geometry is implicitly defined by

$$\mathbf{X}_c^0 \in \Gamma_c^0 \text{ if } f(\mathbf{X}) = 0 \text{ and } g(\mathbf{X}, t) > 0, \quad \mathbf{X} \in \Omega_c^0 \quad (2.1)$$

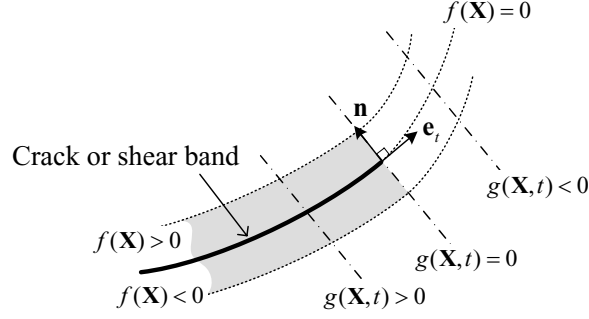


Figure 2.2. A two dimensional discontinuity represented by two implicit functions $f(\mathbf{X})$ and $g(\mathbf{X}, t)$.

For the numerical representation, we approximate the level set function by

$$\sum_I f(\mathbf{X}_I) N_I(\mathbf{X}) = 0 \quad (2.2)$$

where $f(\mathbf{X}) = \min \|\mathbf{X} - \bar{\mathbf{X}}\|_{\bar{\mathbf{X}} \in \Gamma_c}$. As a consequence of Equation (2.2), the surface of discontinuity can be represented by $f(\mathbf{X}_I)$ at the nodes of the cracked elements.

Note that the implicit functions $f(\mathbf{X})$ and $g(\mathbf{X}, t)$ need only to be defined locally around the discontinuity. Furthermore, for elementwise propagation of the discontinuity, we can replace the function $g(\mathbf{X}, t)$ by the set of elements that are cracked or sheared, as shown in Figure 2.3.

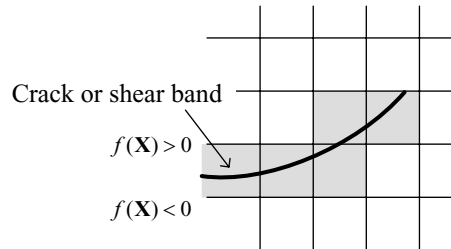


Figure 2.3. The representation of a discontinuity with an implicit functions $f(\mathbf{X})$ for the elementwise propagation of the discontinuity; the function $g(\mathbf{X}, t)$ is replaced by the set of gray elements.

2.1.1. Representation of a discontinuity with phantom nodes

In the following, we will refer specifically to a crack, although the arguments also apply to a shear band. We first illustrate the crack modeling concept in one dimension. Consider a crack at $X = a$ and let the nodes of the element containing the crack be nodes 1 and 2 as shown in Figure 2.4(a). We start with the standard XFEM description of the

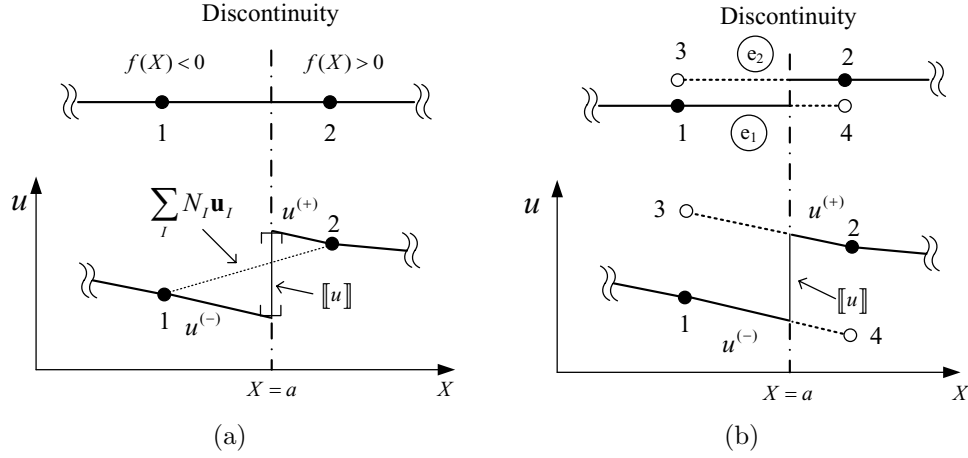


Figure 2.4. A one dimensional representation of a discontinuity by: (a) the standard XFEM and (b) the phantom node method; solid and hollow circles denote the original nodes and the added phantom nodes, respectively.

discontinuous displacement field in an element

$$\mathbf{u}(X, t) = \sum_{I=1}^2 N_I(X) \{ \mathbf{u}_I(t) + \mathbf{q}_I [H(X - a) - H(X_I - a)] \} \quad (2.3)$$

where $H(x)$ is the Heaviside step function given by

$$H(x) = \begin{cases} 1 & x > 0 \\ 0 & x \leq 0 \end{cases} \quad (2.4)$$

We will now transform this to a superposed element formulation for the specific case where node 1 is to the left of the discontinuity as shown in Figure 2.4(b); the general transformation is given subsequently. Writing out Equation (2.3) in abbreviated notation, we have

$$u = u_1 N_1 + u_2 N_2 + q_1 N_1 H + q_2 N_2 (H - 1) \quad (2.5)$$

where $H = H(X - a)$. We can rewrite the above equation as

$$u = (u_1 + q_1) N_1 H + u_1 N_1 (1 - H) + (u_2 - q_2) N_2 (1 - H) + u_2 N_2 H \quad (2.6)$$

where we have used the identities $N_1 = N_1 H + N_1 (1 - H)$ and $N_2 = N_2 H + N_2 (1 - H)$.

We now define

$$\text{element 1} \begin{cases} u_1^1 = u_1 \\ u_2^1 = u_2 - q_2 \end{cases} \quad (2.7)$$

$$\text{element 2} \begin{cases} u_1^2 = u_1 + q_1 \\ u_2^2 = u_2 \end{cases} \quad (2.8)$$

where superscripts and subscripts denote the element and node numbers, respectively.

Equation (2.6) can then be rewritten as

$$u = u_1^1 N_1 (1 - H(X - a)) + u_2^1 N_2 (1 - H(X - a)) + u_1^2 N_1 H(X - a) + u_2^2 N_2 H(X - a) \quad (2.9)$$

Thus, we can consider the displacement field to consist of the displacement fields of two elements: element 1, which is only active for $X < a$, because of the terms $(1 - H(X - a))$

and element 2, which is only active for $X > a$ because of the terms $H(X - a)$. The displacement jump across the crack is

$$\begin{aligned}
 \llbracket u \rrbracket_{X=a} &= \lim_{\epsilon \rightarrow 0} [u(X + \epsilon) - u(X - \epsilon)]_{X=a} \\
 &= N_1(a)(u_1^2 - u_1^1) + N_2(a)(u_2^2 - u_2^1) \\
 &= q_1 N_1(a) + q_2 N_2(a)
 \end{aligned} \tag{2.10}$$

From Equation (2.9), we can see that the discontinuous field can be constructed by adding an extra element, element 2 in this case, as shown in Figure 2.4(b). Then two phantom nodes are added: in this case they are u_2^1 and u_1^2 . As shown in Figure 2.4(b), the two parts of the model are completely disjoint except for a cohesive law which relates the traction across the discontinuity to the jump in the displacement.

We start with the conventional XFEM displacement field

$$\mathbf{u}(\mathbf{X}, t) = \sum_{I=1}^{n^N} N_I(\mathbf{X}) \{ \mathbf{u}_I(t) + \mathbf{q}_I[H(f(\mathbf{X})) - H(f(\mathbf{X}_I))] \} \tag{2.11}$$

Expanding the above as we did for the one dimensional case by subdividing each term into parts that are associated with $f(\mathbf{X}) < 0$ and $f(\mathbf{X}) > 0$, we have

$$\mathbf{u} = \sum_{I=1}^{n^N} [\mathbf{u}_I N_I(1 - H) + \mathbf{u}_I N_I H + \mathbf{q}_I(H - H_I) N_I] \tag{2.12}$$

where $H = H(f(\mathbf{X}))$. We now further expand both fields by duplicating them with the multipliers $H_I^- = H(-f(\mathbf{X}_I))$ and $H_I^+ = H(f(\mathbf{X}_I))$, which do not change the fields, and we make use of the fact that $H - H_I = H - 1$ when $H_I^+ \neq 0$ and $H - H_I = H$ when

$H_I^- \neq 0$. So we have

$$\begin{aligned} \mathbf{u} = \sum_{I=1}^{n^N} [& \mathbf{u}_I H_I^+ N_I (1-H) + \mathbf{u}_I H_I^- N_I (1-H) + \mathbf{u}_I H_I^+ N_I H + \mathbf{u}_I H_I^- N_I H \\ & + \mathbf{q}_I H_I^+ N_I (H-1) + \mathbf{q}_I H_I^- N_I H] \end{aligned} \quad (2.13)$$

We then rewrite the above as

$$\mathbf{u} = \sum_{I=1}^{n^N} [(\mathbf{u}_I - \mathbf{q}_I) H_I^+ N_I (1-H) + \mathbf{u}_I H_I^- N_I (1-H) + \mathbf{u}_I H_I^+ N_I H + (\mathbf{u}_I + \mathbf{q}_I) H_I^- N_I H] \quad (2.14)$$

If we then let

$$\mathbf{u}_I^1 = \begin{cases} \mathbf{u}_I & \text{if } f(\mathbf{X}_I) < 0 \\ \mathbf{u}_I - \mathbf{q}_I & \text{if } f(\mathbf{X}_I) > 0 \end{cases} \quad (2.15)$$

$$\mathbf{u}_I^2 = \begin{cases} \mathbf{u}_I + \mathbf{q}_I & \text{if } f(\mathbf{X}_I) < 0 \\ \mathbf{u}_I & \text{if } f(\mathbf{X}_I) > 0 \end{cases} \quad (2.16)$$

then we can write the displacement field as

$$\mathbf{u}(\mathbf{X}, t) = \sum_{I \in S_1} \underbrace{\mathbf{u}_I^1(t) N_I(\mathbf{X})}_{\mathbf{u}^1(\mathbf{X}, t)} H(-f(\mathbf{X})) + \sum_{I \in S_2} \underbrace{\mathbf{u}_I^2(t) N_I(\mathbf{X})}_{\mathbf{u}^2(\mathbf{X}, t)} H(f(\mathbf{X})) \quad (2.17)$$

where S_1 and S_2 are the index sets of the nodes of superposed element 1 and 2, respectively. As can be seen from Figure 2.5, each element contains original real nodes and phantom nodes. Thus the XFEM field for a completely cut element can be written as the sum of two element fields; one, $\mathbf{u}^1(\mathbf{X}, t)$, which holds for $f(\mathbf{X}) < 0$ and the other, $\mathbf{u}^2(\mathbf{X}, t)$, which holds for $f(\mathbf{X}) > 0$. This form corresponds to the concept proposed by Hansbo and Hansbo [31], though they did not present it in this form. It was previously pointed out

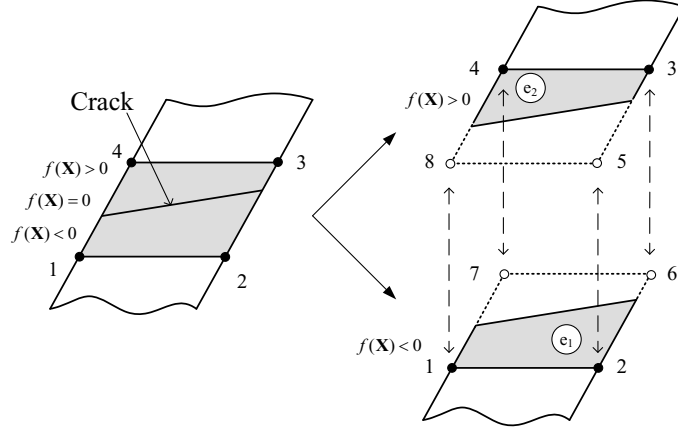


Figure 2.5. The decomposition of a cracked two dimensional element with generic nodes 1 to 4 into two elements e_1 and e_2 ; solid and hollow circles denote the original nodes and the added phantom nodes, respectively.

by Areias and Belytschko [32] that the Hansbo and Hansbo [31] formulation is another form of the XFEM displacement field.

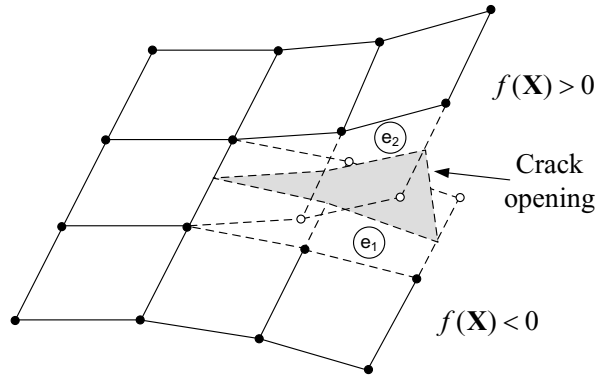


Figure 2.6. The representation of a crack opening with the phantom node method; solid and hollow circles denote the original nodes and the added phantom nodes, respectively.

Note that this equivalence holds for any element, i.e. 3-node triangles, 8-node quadrilaterals, etc. Recasting the discontinuous field in this form simplifies the implementation of the element in existing finite element codes. It is only necessary to add an extra element (i.e. element 2 in this case) and phantom nodes and modify the element quadrature

procedure. The phantom nodes are defined by

$$I \text{ is a phantom node in } \begin{cases} \text{element 1 if } f(\mathbf{X}_I) > 0 \\ \text{element 2 if } f(\mathbf{X}_I) < 0 \end{cases} \quad (2.18)$$

All nodes are integrated in time by the same procedure, as will become clear subsequently.

2.1.2. Representation of a shear band with phantom nodes

The same procedure can be used to model shear bands by adding discontinuities in the tangential component of the displacement in elements crossed by a shear band. Let the tangential direction be denoted by \mathbf{e}_t ; in the context of the level set formulation described here

$$\mathbf{e}_t = \frac{\partial g}{\partial \mathbf{X}} = \nabla_0 g \quad (2.19)$$

where $g(\mathbf{X}, t)$ is a signed distance function. The standard XFEM field for a shear band is then

$$\mathbf{u}(\mathbf{X}, t) = \sum_{I=1}^{n^N} N_I(\mathbf{X}) \{ \mathbf{u}_I(t) + q_I \mathbf{e}_t [H(f(\mathbf{X})) - H(f(\mathbf{X}_I))] \} \quad (2.20)$$

To develop the shear band element, it is necessary to express the normal and tangential components in the nodal displacements, as

$$\mathbf{u}(\mathbf{X}, t) = \sum_{I=1}^{n^N} N_I(\mathbf{X}) \{ \mathbf{u}_{nI}(t) \mathbf{e}_n + \mathbf{u}_{tI}(t) \mathbf{e}_t + q_I \mathbf{e}_t [H(f(\mathbf{X})) - H(f(\mathbf{X}_I))] \} \quad (2.21)$$

where $\mathbf{u}_{nI}(t)$ and $\mathbf{u}_{tI}(t)$ are the normal and tangential components and \mathbf{e}_n is the unit normal to the shear band. Going through the same procedure as before, we obtain

$$\begin{aligned} \mathbf{u} &= \sum_{I=1}^{n^N} \{ \mathbf{e}_t [(\mathbf{u}_{tI} - \mathbf{q}_I) H_I^+ + \mathbf{u}_{tI} H_I^-] + \mathbf{e}_n \mathbf{u}_{nI} \} N_I H(-f(\mathbf{X})) \\ &+ \sum_{I=1}^{n^N} \{ \mathbf{e}_t [(\mathbf{u}_{tI}) H_I^+ + (\mathbf{u}_{tI} + \mathbf{q}_I) H_I^-] + \mathbf{e}_n \mathbf{u}_{nI} \} N_I H(f(\mathbf{X})) \end{aligned} \quad (2.22)$$

We let

$$\mathbf{u}_{tI}^1 = \mathbf{u}_{tI} - \mathbf{q}_I H(f(\mathbf{X}_I)) \quad (2.23)$$

$$\mathbf{u}_{tI}^2 = \mathbf{u}_{tI} + \mathbf{q}_I H(f(\mathbf{X}_I)) \quad (2.24)$$

$$\mathbf{u}_{nI}^1 = \mathbf{u}_{nI}^2 = \mathbf{u}_{nI} \quad (2.25)$$

Then we can write the displacement field $\mathbf{u}(\mathbf{X}, t)$ as the sum of two element displacement fields

$$\mathbf{u}(\mathbf{X}, t) = \mathbf{u}^1(\mathbf{X}, t) + \mathbf{u}^2(\mathbf{X}, t) \quad (2.26)$$

$$\mathbf{u}^1(\mathbf{X}, t) = \sum_{I \in S_1} \mathbf{u}_{tI} N_I H(-f(\mathbf{X})) + \sum_{I=1}^{n^N} \mathbf{u}_{nI} N_I H(-f(\mathbf{X})) \quad (2.27)$$

$$\mathbf{u}^2(\mathbf{X}, t) = \sum_{I \in S_2} \mathbf{u}_{tI} N_I H(f(\mathbf{X})) + \sum_{I=1}^{n^N} \mathbf{u}_{nI} N_I H(f(\mathbf{X})) \quad (2.28)$$

In the shear band elements, phantom degrees of freedom are added only in the tangential direction; the normal components of the nodal displacements correspond to the normal components of the original nodes and are the same in both elements. Consequently, the normal displacement field is also identical in the two elements. The procedure is illustrated

in Figure 2.7, where the phantom degrees of freedom are indicated by dashed lines. The

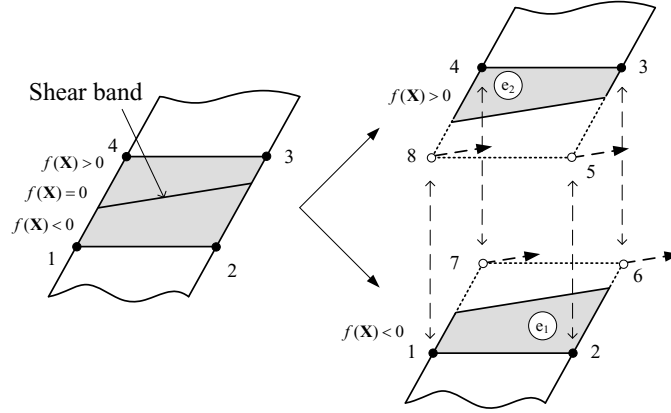


Figure 2.7. The decomposition of a shear element with generic nodes 1 to 4; dashed lines indicate phantom degrees of freedom.

interpretation and its implementation is now somewhat different than for a crack. The construct in Figure 2.5 is replaced by that shown in Figure 2.7 and Equations (2.26)–(2.28). However, as indicated in [22], the modeling of discontinuous tangential fields where the discontinuity is not rectilinear does present certain difficulties. Some of these difficulties arise because we have used C^0 shape functions to describe the discontinuity surface.

2.2. Weak formulation and discretization

2.2.1. Strong form and weak form

We consider a two-dimensional dynamic problem. The strong form of the linear momentum equation in a total Lagrangian description is

$$\frac{\partial P_{ji}}{\partial X_j} + \rho_0 b_i - \rho_0 \ddot{u}_i = 0 \text{ in } \Omega_0 \quad (2.29)$$

where \mathbf{P} is the nominal stress tensor, ρ_0 is the initial mass density, \mathbf{b} is the body force vector.

The boundary conditions are

$$n_j^0 P_{ji} = \bar{t}_i^0 \text{ on } \Gamma_t^0 \quad (2.30)$$

$$u_i = \bar{u}_i \text{ on } \Gamma_u^0 \quad (2.31)$$

$$n_j^0 P_{ji}^- = -n_j^0 P_{ji}^+ = \tau_i^{0c}(\llbracket u_i \rrbracket) \text{ on } \Gamma_c^0 \quad (2.32)$$

where \mathbf{n}^0 is the normal to the indicated boundary, $\boldsymbol{\tau}^{0c}$ is the cohesive traction across the crack, $\bar{\mathbf{t}}^0$ is the applied traction on the Neumann boundary Γ_t and $\bar{\mathbf{u}}$ is the applied displacement on the Dirichlet boundary Γ_u ; $\Gamma_u^0 \cup \Gamma_t^0 = \Gamma^0$, $\Gamma_u \cap \Gamma_t = \emptyset$. Superscript plus and minus signs refer to the two sides of the discontinuity. Indicical notation is used for any lower case indices and repeated subscripts imply summations.

The discrete equations are constructed by the standard Galerkin procedure. The admissible space for the displacement fields is defined as follows:

$$\mathcal{U} = \{\mathbf{u}(\mathbf{X}, t) \mid \mathbf{u}(\mathbf{X}, t) \in \mathcal{H}^1 \text{ in } \Omega \setminus \Gamma_c, \mathbf{u}(\mathbf{X}, t) = \bar{\mathbf{u}}(t) \text{ on } \Gamma_u, \text{ and discontinuous on } \Gamma_c\} \quad (2.33)$$

$$\mathcal{U}_0 = \{\mathbf{u}(\mathbf{X}, t) \mid \mathbf{u}(\mathbf{X}, t) \in \mathcal{H}^1 \text{ in } \Omega \setminus \Gamma_c, \delta \mathbf{u}(\mathbf{X}, t) = 0 \text{ on } \Gamma_u \cup \Gamma_c\} \quad (2.34)$$

The weak form of the momentum equation is given by: for $\mathbf{u}(\mathbf{X}, t) \in \mathcal{U}$

$$\delta W^{\text{kin}} = \delta W^{\text{ext}} - \delta W^{\text{int}} + \delta W^{\text{coh}} \quad \forall \delta \mathbf{u}(\mathbf{X}) \in \mathcal{U}_0 \quad (2.35)$$

where δW^{int} is the internal work, δW^{ext} is the external work performed by applied loads, δW^{kin} is the kinetic work performed by inertia and δW^{coh} is the work performed by the cohesive traction on the crack surface Γ_c . These quantities are defined as (see Belytschko [33] *et al.* for details)

$$\delta W^{\text{kin}} = \int_{\Omega_0} \delta \mathbf{u} \cdot \rho_0 \ddot{\mathbf{u}} \, d\Omega_0 \quad (2.36)$$

$$\delta W^{\text{int}} = \int_{\Omega_0} \frac{\partial \delta \mathbf{u}}{\partial \mathbf{X}} : \mathbf{P} \, d\Omega_0 \quad (2.37)$$

$$\delta W^{\text{ext}} = \int_{\Omega_0} \delta \mathbf{u} \cdot \rho_0 \mathbf{b} \, d\Omega_0 + \int_{\Gamma_t^0} \delta \mathbf{u} \cdot \bar{\mathbf{t}}^0 \, d\Gamma_t^0 \quad (2.38)$$

$$\delta W^{\text{coh}} = - \int_{\Gamma_c} \delta [\![\mathbf{u}]\!] \cdot \boldsymbol{\tau}^c \, d\Gamma_c \quad (2.39)$$

where $\bar{\mathbf{t}}$ is the normalized traction prescribed on Γ_t^0 and $\boldsymbol{\tau}^c$ is the cohesive traction applied on the discontinuity surface; an updated Lagrangian form is used for (2.39).

The finite element discretization of Equation (2.35) yields the discrete form of the momentum equation which leads to

$$\mathbf{f}^{\text{kin}} = \mathbf{f}^{\text{ext}} - \mathbf{f}^{\text{int}} + \mathbf{f}^{\text{coh}} \quad (2.40)$$

where the internal force \mathbf{f}^{int} , the external force \mathbf{f}^{ext} , and the cohesive force \mathbf{f}^{coh} are assembled from element matrices given below. Since the element matrices for uncracked elements are standard, we give them only for a generic pair of elements 1 and 2 crossed by a crack. They are

$$\mathbf{f}_e^{\text{kin}} = \int_{\Omega_0^e} \rho_0 \mathbf{N}^T \mathbf{N} H((-1)^e f(\mathbf{X})) \, d\Omega_0^e \, \ddot{\mathbf{u}}_e \quad (2.41)$$

$$\mathbf{f}_e^{\text{int}} = \int_{\Omega_0^e} \mathbf{B}^T \mathbf{P}_e H((-1)^e f(\mathbf{X})) d\Omega_0^e \quad (2.42)$$

$$\mathbf{f}_e^{\text{ext}} = \int_{\Omega_0^e} \rho_0 \mathbf{N}^T \mathbf{b} H((-1)^e f(\mathbf{X})) d\Omega_0^e + \int_{\Gamma_t^{e0}} \mathbf{N}^T \bar{\mathbf{t}}^0 H((-1)^e f(\mathbf{X})) d\Gamma_t^{e0} \quad (2.43)$$

$$\mathbf{f}_e^{\text{coh}} = (-1)^e \int_{\Gamma_c^{e0}} \mathbf{N}^T \tau^c \mathbf{n}_0 d\Gamma_c^{e0} \quad (2.44)$$

where the subscript e is either 1 or 2, as shown in Figure 2.5, and the superscript e indicates a domain restriction to element e ; \mathbf{B} is the discrete strain-displacement operator.

2.2.2. One point integration scheme with hourglass mode control

To evaluate the integrals Equation (2.41)-(2.43) in the elements in which the Heaviside function appears, a modified numerical quadrature scheme such as subdomain integration is needed [11]. In subdomain integration, the element is subdivided into several subdomains, and each subdomain is integrated separately as shown in Figure 2.8. However,

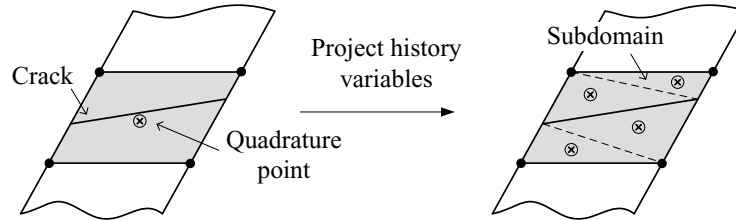


Figure 2.8. Schematic of the conventional subdomain integration scheme for a cracked element.

several difficulties arise in subdomain integration methods when we consider moving discontinuities. For example, in crack or shear band growth in nonlinear materials, the history variables stored at the current quadrature points need to be projected to the newly created quadrature points when a subdomain integration scheme is used.

To circumvent those difficulties, here we adopt a one-point integration scheme in which the Gauss quadrature point is fixed as shown in Figure 2.9. The element uses hourglass

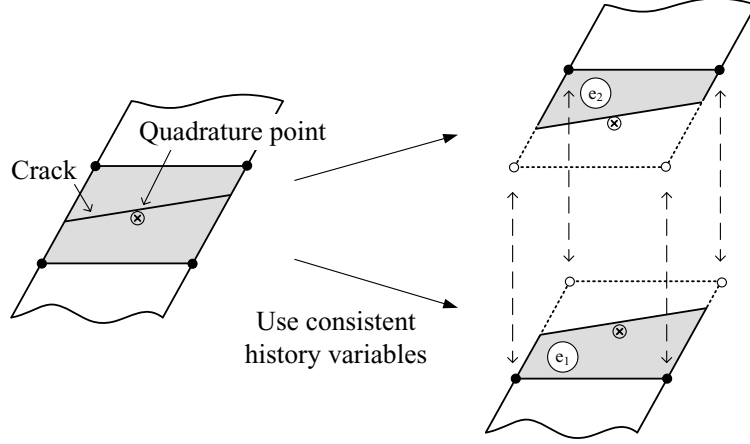


Figure 2.9. Schematic of an one point integration scheme which can provide consistent history variables.

mode control; for details on the hourglass mode control scheme, see [34, 35]. We assume that the stresses are constant within the element and given by the values at the origin of the parent coordinate system.

As we can see from Figure 2.9, the cracked element is replaced by two elements and the nodal forces can be integrated separately as follows:

$$\mathbf{f}_e = \mathbf{f}_{e1} + \mathbf{f}_{e2} \quad (2.45)$$

where \mathbf{f}_e is element force matrix of the cracked element and \mathbf{f}_{e1} and \mathbf{f}_{e2} are the force matrices of newly superposed elements with phantom nodes. Expanding Equations (2.41)-(2.44) yields

$$\mathbf{f}_{(e1/e2)}^{\text{kin}} = \frac{A_{(e1/e2)}}{A_0} \int_{\Omega_0^e} \rho_0 \mathbf{N}^T \mathbf{N} d\Omega_0^e \ddot{\mathbf{u}}_{(e1/e2)} \quad (2.46)$$

$$\mathbf{f}_{(e1/e2)}^{\text{int}} = \frac{A_{(e1/e2)}}{A_0} \int_{\Omega_0^e} \{ \mathbf{B}^T \mathbf{P}_{(e1/e2)} + \mathbf{f}_{(e1/e2)}^{\text{stab}} \} d\Omega_0^e \quad (2.47)$$

$$\mathbf{f}_{e1}^{\text{ext}} = \frac{A_{e1}}{A_0} \int_{\Omega_0^e} \rho_0 \mathbf{N}^T \mathbf{b} d\Omega_0^e + \int_{\Gamma_t^{e0}} H(-f) \mathbf{N}^T \bar{\mathbf{t}}^0 d\Gamma_t^{e0} \quad (2.48)$$

$$\mathbf{f}_{e2}^{\text{ext}} = \frac{A_{e2}}{A_0} \int_{\Omega_0^e} \rho_0 \mathbf{N}^T \mathbf{b} d\Omega_0^e + \int_{\Gamma_t^{e0}} H(f) \mathbf{N}^T \bar{\mathbf{t}}^0 d\Gamma_t^{e0} \quad (2.49)$$

$$\mathbf{f}_{e1}^{\text{coh}} = - \int_{\Gamma_c^{e0}} \mathbf{N}^T \tau^c \mathbf{n}_0 d\Gamma_c^{e0} \quad (2.50)$$

$$\mathbf{f}_{e2}^{\text{coh}} = \int_{\Gamma_c^{e0}} \mathbf{N}^T \tau^c \mathbf{n}_0 d\Gamma_c^{e0} \quad (2.51)$$

where \mathbf{f}^{stab} is a stabilization force matrix to control the hourglass modes, A_0 is the total area of the uncracked element and A_{e1} and A_{e2} are the activated areas of the corresponding superposed elements which consist of regular and phantom nodes. As we can see from Equation (2.46)-(2.49), to compute the force matrix for a cracked element, we only modify it by the area fraction. This computational procedure can be easily implemented within the context of conventional software; it can also be applied to elements with full quadrature.

CHAPTER 3

Phantom Node Method for Shell Problems

Simulation of the fracture of shell structures is engendering considerable interest in the industrial and defense communities. Many components where fracture is of concern, such as windshields, ship hulls, fuel tanks and car bodies are not amenable to three dimensional solid modeling, for the expense would be enormous. Furthermore, fracture is often an important criterion in determining their performance envelopes.

Here, we describe a finite element method based on the extended finite element method (XFEM) [1, 2] for modeling shell structures in explicit finite element programs and illustrate their performance in non-linear problems involving dynamic fracture. The methodology is based on the Hansbo and Hansbo [31] approach, which has previously been applied by Song *et al.* [14] and by Areias *et al.* [16, 17]. The equivalence of the Hansbo and Hansbo [31] basis functions to XFEM [1, 2] is shown in Areias and Belytschko [32]. The method employs an elementwise progression of the crack, i.e. the crack tip is always on an element edge. Réthoré *et al.* [36] have reported that this is usually adequate for dynamic crack propagation. We do not use any near-tip enrichment, although Elguedj *et al.* [37] have achieved good success with near-tip enrichments for static problems.

The literature on dynamic crack propagation in shells is quite limited. Cirak *et al.* [38] have developed an interelement crack method, where the crack is limited to propagation along the element edges. The method is based on the Kirchhoff shell theory. Penalty functions were used to enforce continuity on all interelement edges. Areias and Belytschko

[39] and Areias *et al.* [16, 17] have developed a method for shell fracture based on the extended finite element method for static and implicit time integration.

3.1. Shell formulation with fracture

The discontinuous shell formulation is based on the degenerated shell concept (Ahmad *et al.* [40], and Hughes and Liu [41, 42]), which is almost equivalent to the Mindlin-Reissner formulation when the edges connecting the top and bottom surfaces are normal to the midsurface. We will use a kinematic theory based on the corotational rate-of-deformation and the corotational Cauchy stress rate. These features are briefly summarized in Section 3.2, but are well-known, so we will focus on the modifications needed for the XFEM treatment of fracture.

The velocity field is given by

$$\mathbf{v}(\boldsymbol{\xi}, t) = \mathbf{v}^{mid}(\boldsymbol{\xi}, t) - \zeta \mathbf{e}_3 \times \boldsymbol{\theta}^{mid}(\boldsymbol{\xi}, t) \quad (3.1)$$

where $\mathbf{v}^{mid} \in \mathcal{R}^3$ are the velocities of the shell midsurface, $\boldsymbol{\theta}^{mid} \in \mathcal{R}^3$ are angular velocities of the normals to the midsurface, ζ varies linearly from $-h/2$ to $h/2$ along the thickness, and $\boldsymbol{\xi} = (\xi_1, \xi_2)$ are material coordinates of the manifold that describes the midsurface of the shell; at any point of the shell, we construct tangent unit vectors \mathbf{e}_1 and \mathbf{e}_2 so that

$$\mathbf{e}_3 = \mathbf{e}_1 \times \mathbf{e}_2 \quad (3.2)$$

The nomenclature is illustrated in Figure 3.1.

For the further development of the discontinuous shell formulation, we will limit ourselves to cracks with surfaces normal to the shell midsurfaces as shown in Figure 3.2.

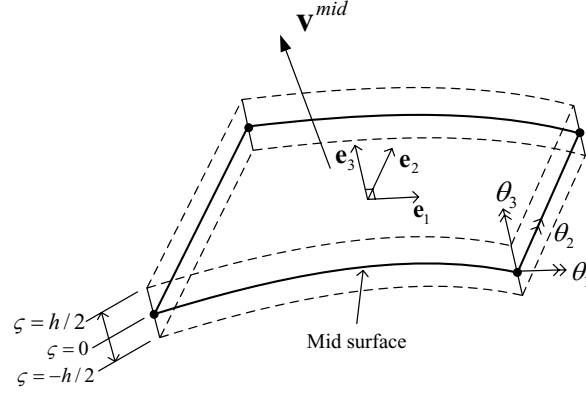


Figure 3.1. The nomenclature for a continuum shell.

Although this is not an intrinsic limitation of the method, it simplifies several aspects of the formulation.

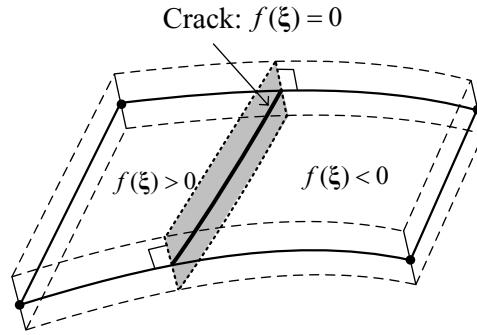


Figure 3.2. Representation of a discontinuity in the reference configuration by a level set function $f(\boldsymbol{\xi})$ in the shell midsurface.

The discontinuous velocity fields due to a crack in any Mindlin-Reissner theory can be described by

$$\mathbf{v}^{mid}(\boldsymbol{\xi}, t) = \mathbf{v}^{cont}(\boldsymbol{\xi}, t) + H(f(\boldsymbol{\xi}))\mathbf{v}^{disc}(\boldsymbol{\xi}, t) \quad (3.3)$$

$$\boldsymbol{\theta}^{mid}(\boldsymbol{\xi}, t) = \boldsymbol{\theta}^{cont}(\boldsymbol{\xi}, t) + H(f(\boldsymbol{\xi}))\boldsymbol{\theta}^{disc}(\boldsymbol{\xi}, t) \quad (3.4)$$

where $f(\boldsymbol{\xi}) = 0$ gives the intersection of the crack surface with the midsurface of the shell and $H(\cdot)$ is the Heaviside function given by

$$H(x) = \begin{cases} 1 & x > 0 \\ 0 & x \leq 0 \end{cases} \quad (3.5)$$

In the above, \mathbf{v}^{cont} and \mathbf{v}^{disc} are continuous functions that are used to model the continuous and the discontinuous parts of the velocity fields, respectively. Similarly, $\boldsymbol{\theta}^{cont}$ and $\boldsymbol{\theta}^{disc}$ are the continuous functions that are used to model continuous and discontinuous parts of the angular velocity fields, respectively. The discontinuities that model the cracks arise from the step function that precedes \mathbf{v}^{disc} and $\boldsymbol{\theta}^{disc}$. It can be seen from Equations (3.1) and (3.3)-(3.4) that these velocity fields can result in a loss of compatibility and in particular material overlap, as indicated in Figure 3.3, when there is a significant discontinuity in the angular motion but the crack opening is small. We will deal with this incompatibility by introducing a penalty in the cohesive law.

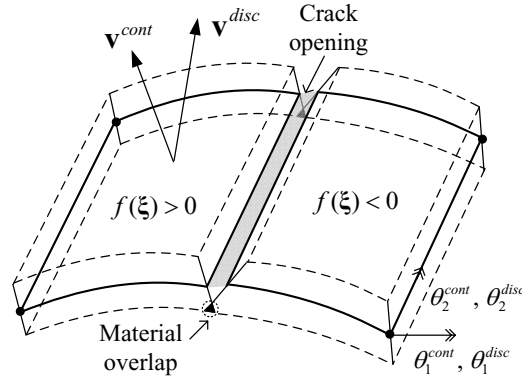


Figure 3.3. Nomenclature of a fractured shell: incompatible material overlapping may occur at the bottom surface due to the opening of the crack.

3.2. Element formulation

The shell element used here is a 4-node shell originally described in [43] with improvements in [44, 14]. The shell element employs an one-point quadrature rule with stabilization [45, 46] for computational efficiency.

When the velocity fields given in Equations (3.3)-(3.4) are specialized to shell finite elements, the continuous part of the corotational velocity components are given by

$$\hat{v}_x(\boldsymbol{\xi}, t) = N_I(\boldsymbol{\xi})\hat{v}_{xI}(t) + \zeta N_I(\boldsymbol{\xi})\hat{\boldsymbol{\theta}}_{yI}(t) \quad (3.6)$$

$$\hat{v}_y(\boldsymbol{\xi}, t) = N_I(\boldsymbol{\xi})\hat{v}_{yI}(t) - \zeta N_I(\boldsymbol{\xi})\hat{\boldsymbol{\theta}}_{xI}(t) \quad (3.7)$$

where N_I are the conventional 4-node finite element bilinear shape functions and the repeated subscripts I denote summation over all nodes. The corotational components of the rate-of-deformation tensor are given by

$$\hat{D}_{ij} = \frac{1}{2} \left(\frac{\partial \hat{v}_i}{\partial \hat{x}_j} + \frac{\partial \hat{v}_j}{\partial \hat{x}_i} \right) \quad (3.8)$$

Substituting Equations (3.6)-(3.7) into (3.8) yields an expression for the rate-of-deformation components

$$\hat{D}_x = \mathbf{b}_{\hat{x}I}\hat{v}_{\hat{x}I} + \zeta(\mathbf{b}_{\hat{x}I}^c \mathbf{v}_{\hat{x}I} + \mathbf{b}_{\hat{x}I}\boldsymbol{\theta}_{yI}) \quad (3.9)$$

$$\hat{D}_y = \mathbf{b}_{\hat{y}I}\hat{v}_{\hat{y}I} + \zeta(\mathbf{b}_{\hat{y}I}^c \mathbf{v}_{\hat{y}I} - \mathbf{b}_{\hat{y}I}\boldsymbol{\theta}_{xI}) \quad (3.10)$$

$$2\hat{D}_{xy} = \mathbf{b}_{\hat{x}I}\hat{v}_{\hat{x}I} + \mathbf{b}_{\hat{y}I}\hat{v}_{\hat{y}I} + \zeta(\mathbf{b}_{\hat{x}I}^c \mathbf{v}_{\hat{x}I} + \mathbf{b}_{\hat{y}I}^c \mathbf{v}_{\hat{y}I} + \mathbf{b}_{\hat{x}I}\boldsymbol{\theta}_{yI} - \mathbf{b}_{\hat{y}I}\boldsymbol{\theta}_{xI}) \quad (3.11)$$

where

$$\begin{Bmatrix} \mathbf{b}_{\hat{x}I} \\ \mathbf{b}_{\hat{y}I} \end{Bmatrix} = \frac{1}{2A} \begin{bmatrix} \hat{y}_{24} & \hat{y}_{31} & \hat{y}_{42} & \hat{y}_{13} \\ \hat{x}_{42} & \hat{x}_{13} & \hat{x}_{24} & \hat{x}_{31} \end{bmatrix} \quad (3.12)$$

$$\begin{Bmatrix} \mathbf{b}_{\hat{x}I}^c \\ \mathbf{b}_{\hat{y}I}^c \end{Bmatrix} = \frac{2\hat{\gamma}_K \hat{z}_K}{A^2} \begin{bmatrix} \hat{x}_{13} & \hat{x}_{42} & \hat{x}_{31} & \hat{x}_{24} \\ \hat{y}_{13} & \hat{y}_{42} & \hat{y}_{31} & \hat{y}_{24} \end{bmatrix} \quad (3.13)$$

and where $\hat{x}_{IJ} = \hat{x}_I - \hat{x}_J$, A is the area of the element and $\hat{\gamma}_K$ is a projection operator, see Belytschko and Bachrach [45]. A state of plane stress is assumed. In Belytschko *et al.* [44], two methods are proposed for the evaluation of \mathbf{b}^c . Here in the equation (3.13), we adopted the \hat{z} method. In this case, curvature is only coupled with the translations for a warped element.

We also have used the shear projection scheme introduced in Belytschko *et al.* [44]. This shear projection scheme gives the components of the transverse shear strain as

$$\hat{D}_{xz} = \mathbf{b}_{x1I}^s \hat{\mathbf{v}}_{zI} + \mathbf{b}_{x2I}^s \hat{\boldsymbol{\theta}}_{xI} + \mathbf{b}_{x3I}^s \hat{\boldsymbol{\theta}}_{yI} \quad (3.14)$$

$$\hat{D}_{yz} = \mathbf{b}_{y1I}^s \hat{\mathbf{v}}_{zI} + \mathbf{b}_{y2I}^s \hat{\boldsymbol{\theta}}_{xI} + \mathbf{b}_{y3I}^s \hat{\boldsymbol{\theta}}_{yI} \quad (3.15)$$

where

$$\begin{Bmatrix} \mathbf{b}_{x1I}^s & \mathbf{b}_{x2I}^s & \mathbf{b}_{x3I}^s \\ \mathbf{b}_{y1I}^s & \mathbf{b}_{y2I}^s & \mathbf{b}_{y3I}^s \end{Bmatrix} = \frac{1}{4} \begin{bmatrix} 2(\bar{x}_{JI} - \bar{x}_{IK}) & (\hat{x}_{JI}\bar{y}_{JI} + \hat{x}_{IK}\bar{y}_{IK}) & -(\hat{x}_{JI}\bar{y}_{JI} + \hat{x}_{IK}\bar{y}_{IK}) \\ 2(\bar{y}_{JI} - \bar{y}_{IK}) & (\hat{y}_{JI}\bar{y}_{JI} + \hat{y}_{IK}\bar{y}_{IK}) & -(\hat{y}_{JI}\bar{y}_{JI} + \hat{y}_{IK}\bar{y}_{IK}) \end{bmatrix} \quad (3.16)$$

and where $(I, J, K) = \{(I, J, K) \mid (1, 2, 4), (2, 3, 1), (3, 4, 1), (4, 1, 3)\}$ and $\bar{x}_{IJ} = \hat{x}_{IJ}/\|\hat{x}_{IJ}\|$.

3.2.1. Representation of the discontinuity

The velocity field of a fractured shell element, which is given by Equations (3.3)-(3.4), can be approximated in the XFEM by

$$\hat{\mathbf{v}}^{mid}(\boldsymbol{\xi}, t) = N_I(\boldsymbol{\xi})\hat{\mathbf{v}}_I^{cont}(t) + H(f(\boldsymbol{\xi}))N_I(\boldsymbol{\xi})\hat{\mathbf{v}}_I^{disc}(t) \quad (3.17)$$

$$\hat{\boldsymbol{\theta}}^{mid}(\boldsymbol{\xi}, t) = N_I(\boldsymbol{\xi})\hat{\boldsymbol{\theta}}_I^{cont}(t) + H(f(\boldsymbol{\xi}))N_I(\boldsymbol{\xi})\hat{\boldsymbol{\theta}}_I^{disc}(t) \quad (3.18)$$

However, when element-wise crack propagation is employed, we have found that it is simpler to program the implementation in the Hansbo and Hansbo [31] form, as developed by Song *et al.* [14]. An element completely cut by a crack is represented by a set of overlapping elements with added phantom nodes as shown in Figure 3.4. The discontinuous

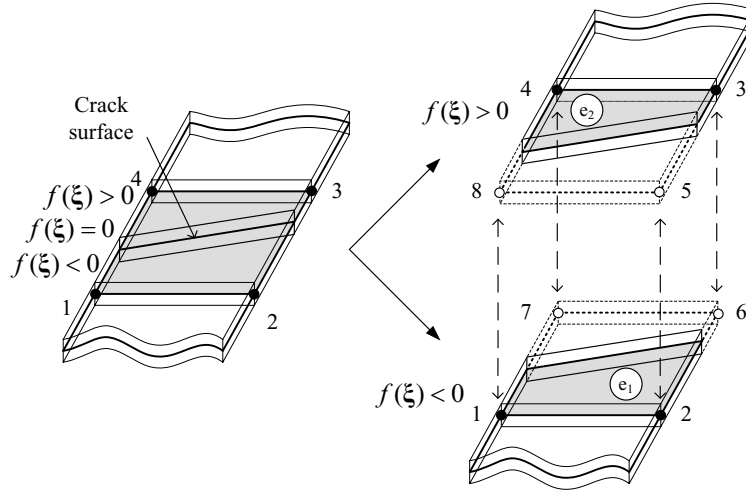


Figure 3.4. The decomposition of a cracked shell element with generic nodes 1–4 into two elements e_1 and e_2 ; solid and hollow circles denote the original nodes and the added phantom nodes, respectively.

velocity field is then constructed by two superimposed velocity fields:

$$\hat{\mathbf{v}}(\boldsymbol{\xi}, t) = \hat{\mathbf{v}}^{e_1}(\boldsymbol{\xi}, t) + \hat{\mathbf{v}}^{e_2}(\boldsymbol{\xi}, t) \quad (3.19)$$

$$= \sum_{I \in S_1} N_I(\boldsymbol{\xi}) H(-f(\boldsymbol{\xi})) \hat{\mathbf{v}}_I^{e_1}(t) + \sum_{I \in S_2} N_I(\boldsymbol{\xi}) H(f(\boldsymbol{\xi})) \hat{\mathbf{v}}_I^{e_2}(t)$$

$$\hat{\boldsymbol{\theta}}(\boldsymbol{\xi}, t) = \hat{\boldsymbol{\theta}}^{e_1}(\boldsymbol{\xi}, t) + \hat{\boldsymbol{\theta}}^{e_2}(\boldsymbol{\xi}, t) \quad (3.20)$$

$$= \sum_{I \in S_1} N_I(\boldsymbol{\xi}) H(-f(\boldsymbol{\xi})) \hat{\boldsymbol{\theta}}_I^{e_1}(t) + \sum_{I \in S_2} N_I(\boldsymbol{\xi}) H(f(\boldsymbol{\xi})) \hat{\boldsymbol{\theta}}_I^{e_2}(t)$$

where S_1 and S_2 are the sets of the nodes of the overlapping element e_1 and e_2 , respectively. Note that velocity fields $\hat{\mathbf{v}}^{e_1}(\boldsymbol{\xi}, t)$ and $\hat{\mathbf{v}}^{e_2}(\boldsymbol{\xi}, t)$ (or $\hat{\boldsymbol{\theta}}^{e_1}(\boldsymbol{\xi}, t)$ and $\hat{\boldsymbol{\theta}}^{e_2}(\boldsymbol{\xi}, t)$) are non-zero only for $f(\boldsymbol{\xi}) < 0$ and $f(\boldsymbol{\xi}) > 0$, respectively, due to the Heaviside step function $H(x)$ that appears in the above equations. The phantom nodes are integrated in time by the same central difference explicit method as those of the other nodes.

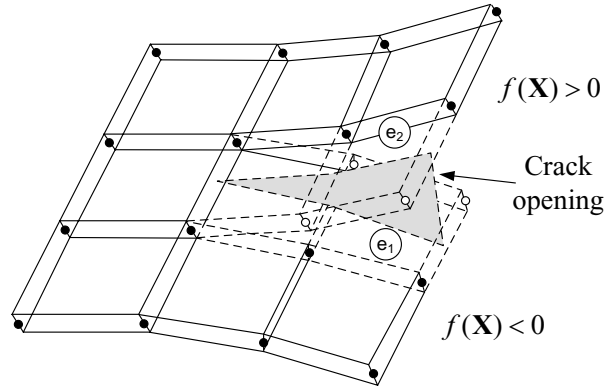


Figure 3.5. Schematic of a crack opening in shell elements with the phantom node method; solid and hollow circles denote the original nodes and the added phantom nodes, respectively.

3.2.2. Representation of multiple discontinuities: crack branching

The concept of the overlapping element method can be easily extended to crack branch modeling. When the original crack, *crack 1*, branches into *crack 1* and *crack 2*, as shown in Figure 3.6, the element in which the crack branches is replaced by three overlapping elements.

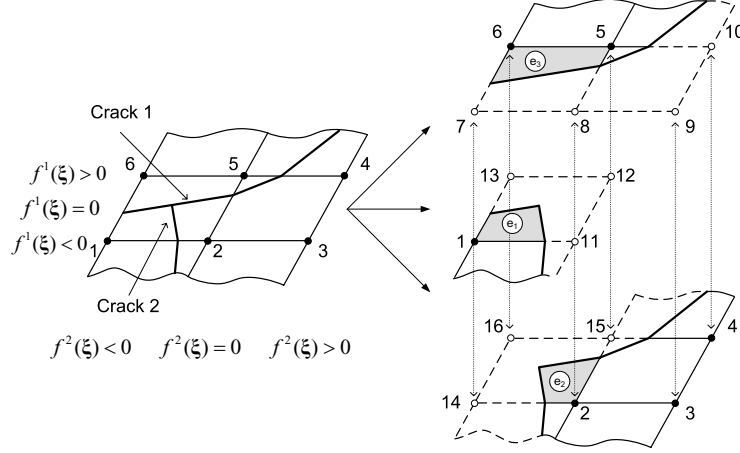


Figure 3.6. The decomposition of an element into three elements e_1 , e_2 and e_3 to model crack branching; solid and hollow circles denote the original nodes and the added phantom nodes, respectively.

Let $f^1(\xi) = 0$ describe the original crack and one branch, and let $f^2(\xi) = 0$ describe the second branch. The discontinuous velocity field is then given by

$$\begin{aligned}
 \hat{\mathbf{v}}(\xi, t) &= \hat{\mathbf{v}}^{e_1}(\xi, t) + \hat{\mathbf{v}}^{e_2}(\xi, t) + \hat{\mathbf{v}}^{e_3}(\xi, t) \\
 &= \sum_{I \in S_1} N_I(\xi) H(-f^1(\xi)) H(-f^2(\xi)) \hat{\mathbf{v}}_I^{e_1}(t) \\
 &\quad + \sum_{I \in S_2} N_I(\xi) H(-f^1(\xi)) H(f^2(\xi)) \hat{\mathbf{v}}_I^{e_2}(t) \\
 &\quad + \sum_{I \in S_3} N_I(\xi) H(f^1(\xi)) H(-f^2(\xi)) \hat{\mathbf{v}}_I^{e_3}(t)
 \end{aligned} \tag{3.21}$$

The element nodal forces are developed as in Belytschko *et al.* [43]. In addition, curvature-translation coupling terms are added and a shear projection operator replaces the previous transverse shear terms. The principle of virtual power is used to derive the relationship for the internal nodal forces. The principle states that:

$$\delta\mathcal{P}^{\text{int}} = \underbrace{A(\mathbf{B}_m\delta\mathbf{v})^T \begin{Bmatrix} \hat{f}_x^r \\ \hat{f}_y^r \\ \hat{f}_{xy}^r \end{Bmatrix}}_{\text{virtual membrane power}} + \underbrace{A(\mathbf{B}_b\delta\mathbf{v})^T \begin{Bmatrix} \hat{m}_x^r \\ \hat{m}_y^r \\ \hat{m}_{xy}^r \end{Bmatrix}}_{\text{virtual bending power}} + \underbrace{\bar{\kappa}A(\mathbf{B}_s\delta\mathbf{v})^T \begin{Bmatrix} \hat{f}_{xz}^r \\ \hat{f}_{yz}^r \end{Bmatrix}}_{\text{virtual transverse shear power}} \quad (3.22)$$

where $\bar{\kappa}$ is the shear reduction factor from the Mindlin shell theory, and \hat{f}_{ij}^r and \hat{m}_{ij}^r are the resultant forces and moments which are integrated through the element thickness.

$$\hat{f}_{ij}^r = \int \hat{\sigma}_{ij} d\hat{z} \quad (3.23)$$

$$\hat{m}_{ij}^r = \int \hat{z} \hat{\sigma}_{ij} d\hat{z} \quad (3.24)$$

where $\hat{z} = \zeta \frac{h}{2}$.

We substitute Equations (3.9)-(3.16) into (3.22) and invoking the arbitrariness of $\delta\mathbf{v}$ yields the discretized element nodal forces:

$$\hat{f}_{xI}^{\text{int}} = A_e (b_{xI} \hat{f}_x^r + b_{yI} \hat{f}_{xy}^r + b_{xI}^c \hat{m}_x^r + b_{yI}^c \hat{m}_{xy}^r) \quad (3.25)$$

$$\hat{f}_{yI}^{\text{int}} = A_e (b_{yI} \hat{f}_y^r + b_{xI} \hat{f}_{xy}^r + b_{yI}^c \hat{m}_y^r + b_{xI}^c \hat{m}_{xy}^r) \quad (3.26)$$

$$\hat{f}_{zI}^{\text{int}} = A_e \bar{\kappa} (b_{x1I}^s \hat{f}_{xz}^r + b_{y1I}^s \hat{f}_{yz}^r) \quad (3.27)$$

$$\hat{m}_{xI}^{\text{int}} = A_e [\bar{\kappa} (b_{x2I}^s \hat{f}_{xz}^r + b_{y2I}^s \hat{f}_{yz}^r) - (b_{yI} \hat{m}_y^r + b_{xI} \hat{m}_{xy}^r)] \quad (3.28)$$

$$\hat{m}_{yI}^{int} = A_e [\bar{\kappa}(b_{x3I}^s \hat{f}_{xz}^r + b_{y3I}^s \hat{f}_{yz}^r) + (b_{xI} \hat{m}_x^r + b_{yI} \hat{m}_{xy}^r)] \quad (3.29)$$

$$\hat{m}_{zI}^{int} = 0 \quad (3.30)$$

The final form of the element internal forces in the global coordinates can be determined by performing the transformation between the corotational and global coordinates as below:

$$\mathbf{f}_e^{int} = \mathbf{T}_e^T (\hat{\mathbf{f}}_e^{int} + \hat{\mathbf{f}}_e^{stab}) \quad (3.31)$$

where \mathbf{T} is the transformation matrix between global and corotational components and $\hat{\mathbf{f}}_e^{int}$ is the nodal internal force vector in the corotational coordinate systems. In Equation (3.31), to circumvent the rank deficiency due to one point integration, an hourglass control force, $\hat{\mathbf{f}}_e^{stab}$, is added to the internal force vector. For a description of the hourglass control scheme, see [44, 45].

For each of the overlapped elements modeling a crack, the nodal forces are given by

$$\mathbf{f}_e^{int} = \left(\sum_{k=1}^{N_{ele}^{ovr}} \frac{A_{e_k}}{A_e} \mathbf{T}_{e_k}^T \hat{\mathbf{f}}_{e_k}^{int} \right) + \mathbf{T}_e^T \hat{\mathbf{f}}_e^{stab} \quad (3.32)$$

where N_{ele}^{ovr} is the total number of overlapped elements, A_{e_k} is the activated area of the corresponding overlapping elements in the corotational coordinates, \mathbf{f}_e is the nodal force vector of a cracked element and $\hat{\mathbf{f}}_{e_k}$ is the corotational nodal force vector of the overlapped element e_k . Note that the internal nodal forces of elements e_k can be calculated by multiplying Equations (3.25)-(3.30) by the area fraction, A_{e_k}/A_e . A more detailed discussion of the concept of the modification of cracked element nodal forces by area fractions can be found in Song *et al.* [14].

CHAPTER 4

Constitutive Models and Continuous-Discontinuous Transition

In this chapter, we will briefly review some of the constitutive models that are used in this work. Also, we will describe proposed fracture criteria which are suitable for numerical computations with low order element within the framework of explicit dynamic methods and we also describe the cohesive law which is used to model fracture energy dissipation.

A cohesive crack model is prescribed along the newly injected strong discontinuity surfaces until the crack opening is fully developed, i.e. cohesive traction has vanished. The roles of the cohesive model are:

- (i) To remedy spurious mesh-dependent pathological behavior by providing a bounded solution at the crack tip. For linear elastic fracture simulations, if the crack tip is not smoothly closed with cohesive forces, finite element solutions are unbounded at the crack tip due to the crack tip stress singularity and a crack path is depends strongly on the surrounding mesh resolution. Also, for fracture in plastic bulk materials, the crack tip stress singularity can be slightly alleviated by plasticity. However, the finite element solutions still depend on the mesh resolution.
- (ii) To ensure an accurate dissipation of energy due to fracture. If the crack opening displacement is not governed by a cohesive model, the normal component of the stress along the crack surface can suddenly drop to zero due to lack of fracture

energy dissipation; note that injecting a strong discontinuity without including a cohesive force is the same as creating two free surfaces without dissipating additional surface energy. In this case, the total system suffers from an excessive accumulation of elastic energy and this excessive energy accelerates the crack propagation speed: for details on the relationship between crack propagation speed and dissipated fracture energy, refer to Song *et al.* [26] and Rabczuk *et al.* [47].

4.1. Constitutive models

4.1.1. Material damage model

One of the material models used for this work is the damage model of Lemaitre [48]. In this model, a scalar damage parameter D represents the extent of damage. This constitutive model was used only for small displacement problems, so the constitutive relation is given as:

$$\sigma_{ij} = (1 - D)C_{ijkl}\epsilon_{kl} \quad (4.1)$$

where D can have values from 0 to 1, C_{ijkl} is the elastic modulus of the undamaged material, and σ_{ij} and ϵ_{kl} are the Cauchy stress and linear strain, respectively. As can be seen from Equation (4.1), an increase in damage parameter D leads to a softer material response. The damage evolution law is given by

$$D(\bar{\epsilon}) = 1 - (1 - A)\epsilon_{D_0}\bar{\epsilon}^{-1} - Ae^{-B\langle\bar{\epsilon}-\epsilon_{D_0}\rangle} \quad (4.2)$$

where $\bar{\epsilon}$ is the effective strain, A and B are material parameters and ϵ_{D_0} is the strain threshold. The effective strain $\bar{\epsilon}$ is defined as

$$\bar{\epsilon} = \sqrt{\sum_{i=1}^3 \langle \epsilon_i \rangle^2} \quad (4.3)$$

where ϵ_i is the i^{th} principal strain and $\langle \cdot \rangle$ is the Macaulay bracket. Note that in Equation (4.3), the compressive strain components are filtered out by the Macaulay bracket and therefore do not contribute to the damage.

4.1.2. Hardening plasticity for quasi-brittle material

We employed a von-Mises type hardening J_2 -plasticity model for quasi-brittle materials. For the integration of the constitutive model we used a first-order forward Euler explicit integration scheme. In the simulation of fracture within the explicit simulation framework, the integration time step is limited to a small fraction of the critical time step, which is usually smaller than the critical time step for the integration of the constitutive equation.

The rate form of the constitutive equation in the corotational coordinate system is given by

$$\frac{D\hat{\boldsymbol{\sigma}}}{Dt} = \hat{\mathbf{C}}^{elas} : (\hat{\mathbf{D}} - \hat{\mathbf{D}}^p) \quad (4.4)$$

where, $\hat{\boldsymbol{\sigma}}$ is the corotational rate of Cauchy stress, $\hat{\mathbf{C}}^{elas}$ is the corotational elastic moduli tensor and $\hat{\mathbf{D}}^p$ is the corotational rate of plastic deformation tensor. For a von-Mises material with isotropic hardening, the plastic corotational rate of deformation tensor is given by

$$\hat{\mathbf{D}}^p = \mathbf{r} \dot{\lambda} = \mathbf{r} \frac{\mathbf{r} : \hat{\mathbf{C}}^{elas} : \hat{\mathbf{D}}}{\mathbf{r} : \hat{\mathbf{C}}^{elas} : \mathbf{r} + h_p} \quad (4.5)$$

where \mathbf{r} is J_2 plasticity flow direction, $\dot{\lambda}$ is plastic flow rate parameter, and h_p is the plastic hardening modulus.

4.1.3. Thermo elasto-viscoplasticity

For ductile fracture and shear band simulations, we used a thermo-elasto-viscoplastic constitutive model in which heat conduction is neglected for simplicity. The rate form of the constitutive equation is given by

$$\overset{\nabla}{\boldsymbol{\tau}} = \mathbf{C}^{elas} : (\mathbf{D} - \mathbf{D}^{vp} - \mathbf{D}^t) \quad (4.6)$$

where, $\overset{\nabla}{\boldsymbol{\tau}}$ is the Jaumann rate of Kirchhoff stress, \mathbf{C}^{elas} is the elastic moduli tensor, \mathbf{D}^{vp} is the viscoplastic rate of deformation and \mathbf{D}^t is the thermal rate of deformation. For a von-Mises material with isotropic hardening condition, the viscoplastic rate of deformation, \mathbf{D}^{vp} , is given by

$$\mathbf{D}^{vp} = \frac{3\dot{\bar{\epsilon}}}{2\bar{\sigma}} \boldsymbol{\tau}' \quad (4.7)$$

where, $\boldsymbol{\tau}'$ is the deviatoric part of Kirchhoff stress and $\bar{\sigma}$ is the effective stress. $\dot{\bar{\epsilon}}$ is the effective plastic strain rate which is characterized by the power law relation

$$\dot{\bar{\epsilon}} = \dot{\epsilon}_0 \left[\frac{\bar{\sigma}}{g(\bar{\epsilon}, T)} \right]^m \quad (4.8)$$

where m is a power index which indicates the rate sensitivity of the material and $g(\bar{\epsilon}, T)$ is the material hardening or softening parameter. In this study $g(\bar{\epsilon}, T)$ is given by

$$g(\bar{\epsilon}, T) = \sigma_0 \left[1 + \frac{\bar{\epsilon}}{\epsilon_0} \right]^N \left\{ 1 - \delta \left[\exp\left(\frac{T - T_0}{k}\right) - 1 \right] \right\} \quad (4.9)$$

The details about the constitutive equation can be found in Perzyna [49], Lemonds and Needleman [50], Zhou *et al.* [51] and Li *et al.* [52]. The thermal rate of deformation, \mathbf{D}^t , is given as

$$\mathbf{D}^t = \alpha \dot{T} \mathbf{I} \quad (4.10)$$

where α is coefficient of the thermal expansion. For adiabatic heating, we have

$$\rho_0 C_p \dot{T} = \chi \boldsymbol{\tau} : \mathbf{D}^{vp} \quad (4.11)$$

where χ is the fraction of plastic work converted to heat. For the explicit stress update algorithm, we employed the rate tangent modulus algorithm given by Peirce *et al.* [53].

4.2. Continuum to discontinuity transition

4.2.1. Maximum tensile principle strain criterion

A strain based fracture criterion was used to determine the onset point of a post strain localization behavior of a material, i.e. fracture. When the strain at a crack tip material point reaches a fracture threshold, we inject a strong discontinuity at the previous crack tip according to maximum principal tensile strain direction of an averaged strain, $\boldsymbol{\epsilon}^{avg}$. We use a nonlocal (i.e. surface weighted average) scheme to compute the averaged strain, $\boldsymbol{\epsilon}^{avg}$, which is given by

$$\boldsymbol{\epsilon}^{avg} = \frac{4}{\pi} \int_{-\frac{\pi}{2}}^{\frac{\pi}{2}} \int_0^{r_c} w(r) \boldsymbol{\epsilon} \, dr \, d\theta \quad (4.12)$$

where r and θ are the distance from the crack tip and the angle with the tangent to the crack path, respectively, and $w(r)$ is a weight function; for the latter, we use a cubic spline

function given by

$$w(r) = \begin{cases} 4\left(\frac{r}{r_c} - 1\right)\left(\frac{r}{r_c}\right)^2 + \frac{2}{3} & 0 < r < 0.5 r_c \\ \frac{4}{3}\left(1 - \frac{r}{r_c}\right)^3 & 0.5 r_c \leq r \leq r_c \\ 0 & \text{otherwise} \end{cases} \quad (4.13)$$

where $r_c (\simeq 3h_e)$ is the characteristic size of the averaging domain. A typical averaging domain is shown in Figure 4.1.

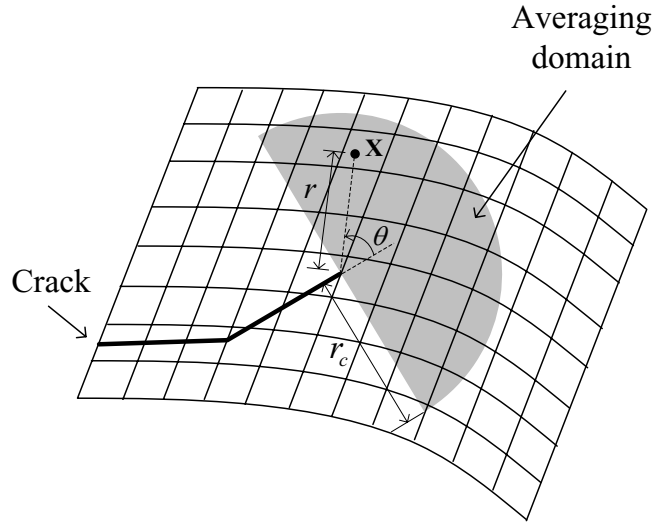


Figure 4.1. Schematic of the averaging domain with a radius of r_c .

4.2.2. Material stability criterion

The discontinuous crack or shear band model is initiated when the material loses stability. In a rate-independent material, loss of stability coincides with loss of hyperbolicity and the conditions are well known; for examples, see Belytschko *et al.* [11].

However, in a rate-dependent material, hyperbolicity is not lost, so the transition to a discontinuity is governed by material instability. Material instability can be determined

by examining whether growth occurs in an initially stressed infinite body perturbed by a harmonic field (see, Belytschko [33], p. 386)

$$\tilde{\mathbf{u}} = \mathbf{h}_1 \cdot e^{at} \cdot e^{i(bt+k\mathbf{h}_2 \cdot \mathbf{X})} \quad (4.14)$$

where \mathbf{h}_1 is the polarization direction, \mathbf{h}_2 is the direction of the wave propagation, k is the wave number and a is a real number that determines the stability of the response; if $a > 0$ the response is unstable. The conditions that $a < 0$ coincides with the condition that

$$\mathbf{h}_1 \otimes \mathbf{h}_2 : \mathcal{A} : \mathbf{h}_1 \otimes \mathbf{h}_2 < 0 \quad \forall \mathbf{h}_i \quad (4.15)$$

where \mathcal{A} relates the rate of stress to the rate of strain. At the point that there exist \mathbf{h}_i such that Equation (4.15) is violated, a discontinuity is introduced such that $\nabla \mathbf{f}$ is parallel to \mathbf{h}_2 .

4.3. Cohesive crack models

In this study, we prescribed only the normal traction of a linear cohesive model, as shown in Figure 4.2, since crack propagation is usually due to mode I fracture in quasi-brittle materials.

The cohesive model is constructed so that the dissipated energy due to the crack propagation is equivalent to the fracture energy:

$$G_f = \int_0^{\delta_{\max}} \tau_c(\delta_n) d\delta = \frac{1}{2} \tau_{\max} \delta_{\max} \quad (4.16)$$

where δ_{\max} is the maximum crack opening displacement, G_f is the fracture energy, and δ_n is the jump in the displacement normal to the crack surface, Γ_d , as shown in Figure

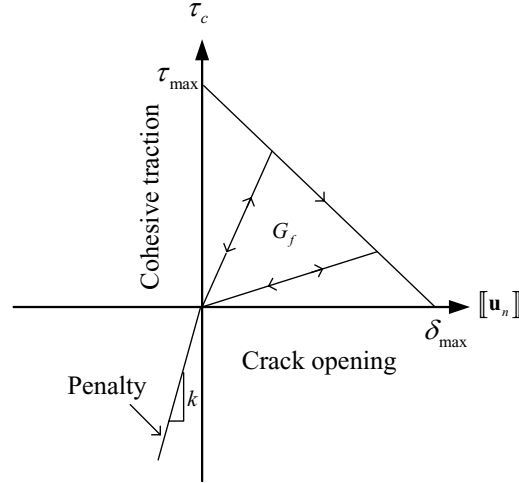


Figure 4.2. Schematic of a linear cohesive law: the area under the curve is the fracture energy, G_f .

4.2. In addition, a penalty force was added in compression. This penalty force depends only on δ_n and is given by $\tau_c = k\delta_n$ when $\delta_n < 0$.

CHAPTER 5

Numerical Examples

5.1. Dynamic fracture of two dimensional planes

5.1.1. Edge-cracked plate under impulsive loading

These simulations concern the experiment reported by Kalthoff and Winkler [54] in which a plate with two initial edge notches is impacted by a projectile as shown in Figure 5.1(a). In the experiment, two different failure modes were observed by modifying the projectile speed; at high impact velocities, ductile failure with a shear band propagation is observed to emanate from the notch at an angle of -10° with respect to initial notch, whereas at lower strain rates, brittle failure with a crack propagation angle of about 70° is observed. In this study, we consider both failure modes.

To take advantage of the twofold symmetry of the configuration, only the upper half of the plate is modeled, as shown in Figure 5.1(b): at the bottom edge of the finite element model, the boundary conditions are $u_y = 0$ and $t_x = 0$. The initial impact velocity, \bar{v} , is applied to the left edge of the plate along the segment $0 \leq y \leq 25$ mm. We assumed that the projectile has the same elastic impedance as the specimen, so we applied one half of the projectile speed, $\bar{v} = 16.5$ m/s for the brittle fracture mode and $\bar{v} = 32.0$ m/s for the ductile shear mode, to the left edge as an initial condition (see, [55, 56]). The initial notch was modeled by including two lines of nodes separated by $300 \mu\text{m}$. The material is a maraging steel 18Ni1900 [57] and its material properties are $\rho = 8000 \text{ kg/m}^3$,

$E = 190$ GPa and $\nu = 0.30$. The initial Rayleigh wave speed is $c_R = 2799.2$ m/s. We used a central difference time integration scheme with a Courant number of 0.1.

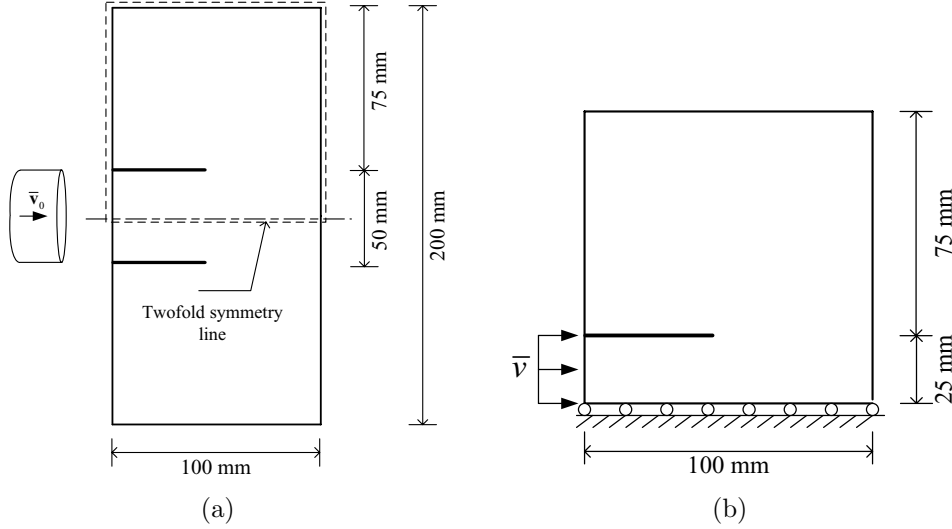


Figure 5.1. Setup for the edge-cracked plate problem under impact loading: (a) the original experimental setup and (b) its numerical model.

5.1.1.1. Dynamic crack propagation with a damage model. We considered a Lemaitre damage constitutive model [58] with $A = 1.0$, $B = 200.0$ and $\varepsilon_{D_0} = 3.0 \times 10^{-3}$. A linear cohesive crack model with fracture energy $G_F = 2.213 \times 10^4$ N/m was used. Numerical simulations were made with two different meshes to observe mesh sensitivity: 50×50 and 100×100 meshes.

The results for the 100×100 mesh and a comparison of the results of the 50×50 and 100×100 meshes are shown in Figure 5.2 and Figure 5.3, respectively. Both simulations are concluded at around $80 \mu\text{s}$ when the crack tip reaches the upper boundary. Both results show very similar trajectories for the crack. The initial crack propagation angle is around 64° and the average angle from the initial crack tip to the final crack tip is about 60° for both meshes; the crack path is nearly straight. This angle is 10° smaller

than the observed angle [54] and the angle obtained by meshfree [59, 60] and XFEM [36]. In the latter, the crack tip singularity was included as an enrichment at the notch. Evidently, due to approximation errors of constant strain elements, the near tip field is not reproduced well enough to yield a highly accurate direction for crack propagation. However, for most engineering purposes, the accuracy is more than adequate. There are damaged areas in the bottom right corner of the model due to wave reflection.

The crack propagation speed is shown in Figure 5.4. The crack tip speed never exceeds the Rayleigh wave speed 2799.2 m/s. For the 50×50 mesh, the crack tip speed is substantially higher than reported in Belytschko *et al.* [11]; in the reference [11], the method that modeled crack progression within the element was used. This suggests that elementwise propagation of the crack introduces some errors in crack tip speed for coarse meshes, and in particular, it appears to increase the predicted crack tip speed. However, the crack tip speed for the 100×100 mesh decreases and agrees better with the computation of Belytschko *et al.* [11]. Note that the crack tip speed is taken to be the average over 5 time steps.

5.1.1.2. Comparisons with the element deletion and the interelement crack methods. Figures 5.5(a) and (b) show the crack paths computed by the element deletion method with structured 100×100 mesh and equivalent unstructured meshes, respectively. In these calculations, we used $G_f = 2.213 \times 10^4$ N/m and $\epsilon_0 = 4.440 \times 10^{-3}$ for a linear elastic-linear softening law where ϵ_0 is the strain at the peak stress. As we can see from Figure 5.5(a), a structured mesh cannot predict the experimental crack path and shows a severe pathological behavior. For an unstructured mesh, the crack first grows vertically

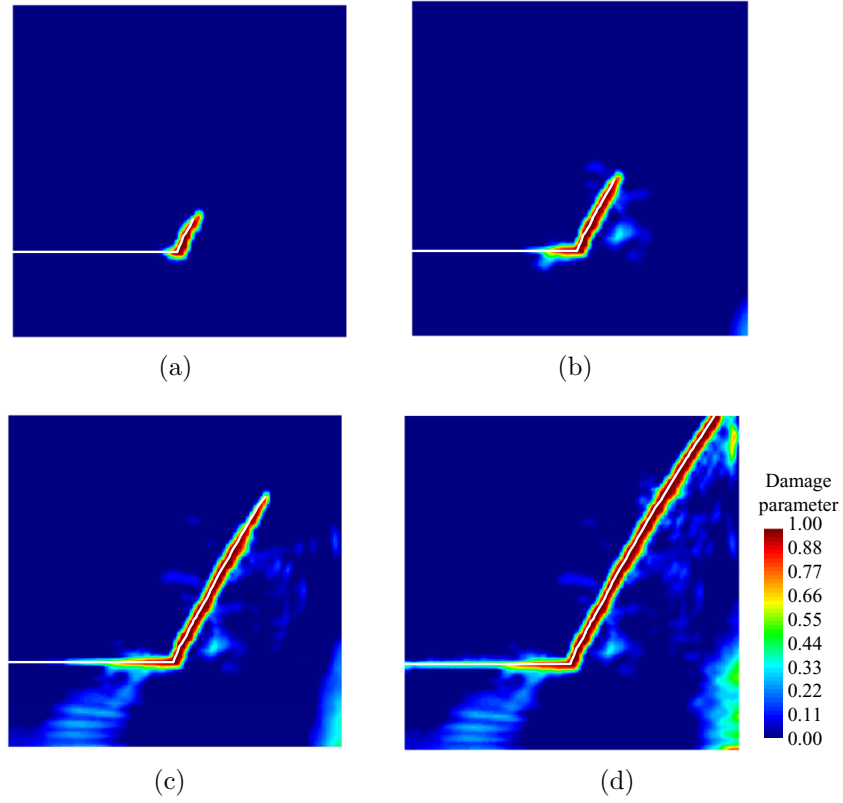


Figure 5.2. The crack path for a 100×100 quadrilateral mesh with a Lemaitre damage model at different time steps: (a) $t = 39.29 \mu\text{s}$, (b) $t = 42.86 \mu\text{s}$, (c) $t = 53.58 \mu\text{s}$ and (d) $t = 88.58 \mu\text{s}$.

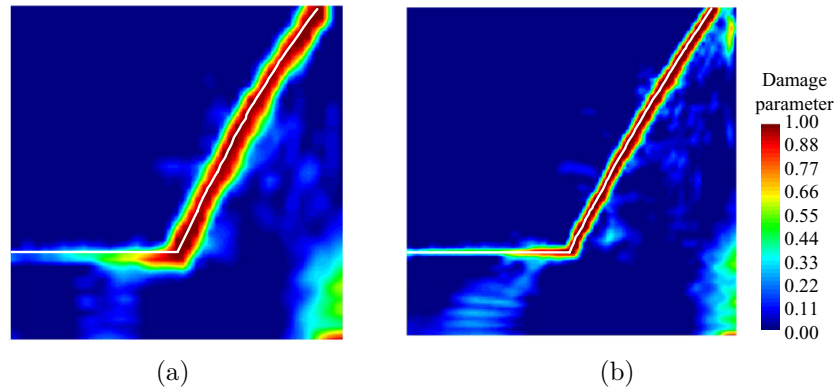


Figure 5.3. Comparison of the crack paths for a 50×50 and a 100×100 quadrilateral meshes with a Lemaitre damage model at $t = 88.58 \mu\text{s}$: (a) a 50×50 quadrilateral mesh and (b) a 100×100 quadrilateral mesh.

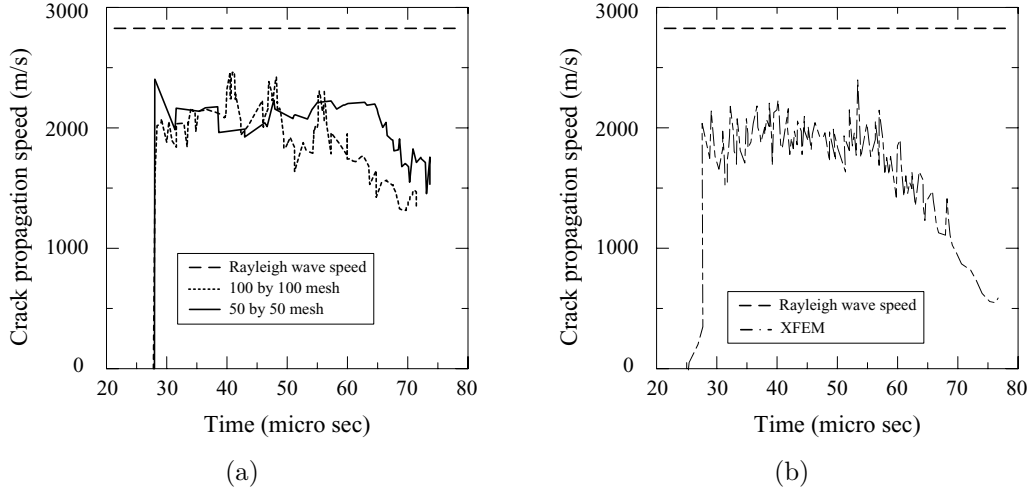


Figure 5.4. Crack propagation speed for the edge-cracked plate problem under impulsive loading: (a) the current method and (b) the previous results in Reference [11]; in Reference [11] a 80×80 cross-triangular mesh was used.

upward and then grows at an angle of 50° . There are fractured areas in the bottom right corner of the model due to wave reflection.

Figures 5.6(a) and (b) show the final crack path by the interelement crack method of the Xu and Needleman [9] with structured 50×50 and 100×100 meshes, respectively. In these calculations, we used $\phi_n = \phi_t = 2.2170 \times 10^4$ J/m², $\delta_n = \delta_t = 4.720 \times 10^{-6}$ m, $r = 0.0$ and $q = 1.0$ for cohesive zone model [9]. For a 100×100 mesh, the crack initially propagates with an angle of 70° , which agrees quite well with the experiment, but after the mid point of the simulation, the crack suddenly propagates at a 45° angle. For the simulation with a 50×50 mesh, there is no shift. The overall crack propagation angle is around 55° . For both meshes, crack paths meander along the 90° and 45° edges to achieve this angle.

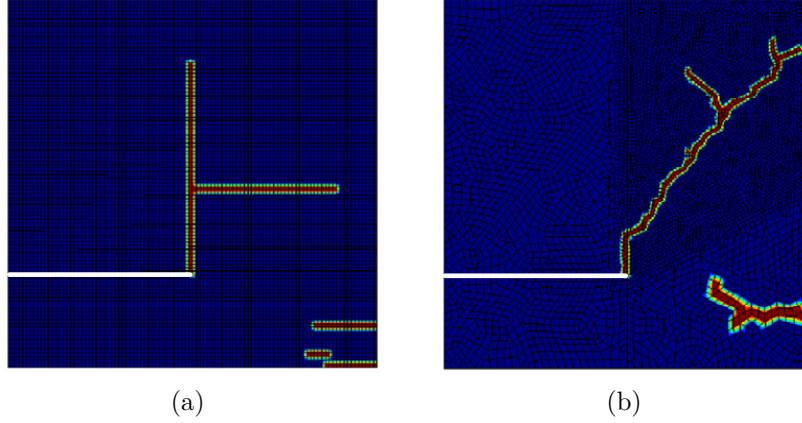


Figure 5.5. Crack paths for the element deletion method with: (a) a 100×100 structured quadrilateral mesh at $t = 60.19 \mu s$ and (b) an unstructured mesh ($h_{avg}^e = 1.0 \text{ mm}$) at $t = 67.85 \mu s$.

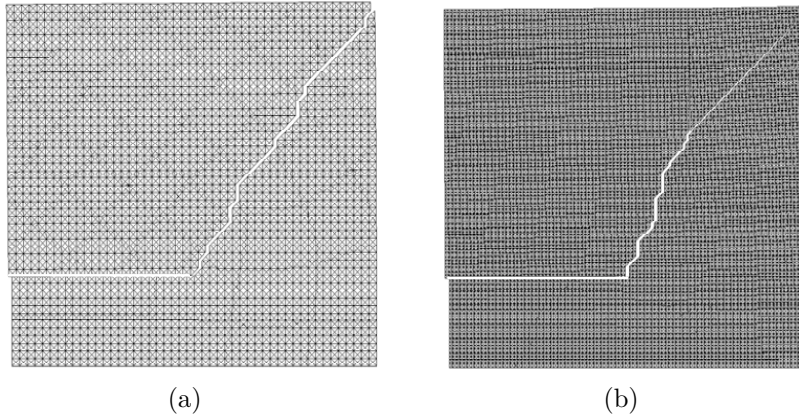


Figure 5.6. The crack paths of the interelement crack method of Xu and Needleman [9] with 50×50 and 100×100 quadrilateral meshes: (a) $t = 98.65 \mu s$ and (b) $t = 98.73 \mu s$.

5.1.1.3. Dynamic crack and shear band propagation with an elasto-viscoplastic model. In this example, we simulate both the brittle and the shear fracture mode of the Kalthoff and Winkler experiment [54]. To observe dynamic shear band propagation, we employed a thermo-elasto-viscoplastic constitutive model [50, 51, 52] with an explicit

stress update algorithm [53]. The material is a maraging steel, 18Ni1900, as in the preceding example and the material properties for the thermo-elasto-viscoplastic constitutive model can be found in reference [51, 52]. For the crack and shear band criterion, as an indicator of the propagation and the direction, the loss of material stability condition is employed. Note that a rate-dependent material such as an elasto-viscoplastic material does not lose hyperbolicity, but lose material stability.

At an initial impact velocity of 16.5 m/s, we observe dynamic crack propagation as in the preceding example. The comparison of the crack growth paths between the results with damage model and elasto-viscoplastic model are shown in Figure 5.7. The crack growth paths of the elasto-viscoplastic model agree better with the experimental results than those for the hypo-elastic constitutive law with damage. The initial crack propagation angle is around 67.4° and the average overall crack propagation angle is 65.1° . This $2 \sim 5^\circ$ discrepancy in the angle with the experiment may be due to the absence of a crack tip stress concentration.

At an initial impact velocity of 32 m/s, the effective plastic strain distribution and a comparison of the shear band path with experimental results are shown in Figure 5.8. We assumed that the shear band energy is $G_F = 100$ N/m. In this study, since we adopted a strong discontinuity approach to represent sheared elements, the localized plastic strain along the shear band is substantially lower than that of the physical shear band. However, as we can observe from Figure 5.8(b), the overall shear band propagation path agrees quite well with the experimental results [56], though the shear band path drifted downward more than the experimental results along the last half of the path.

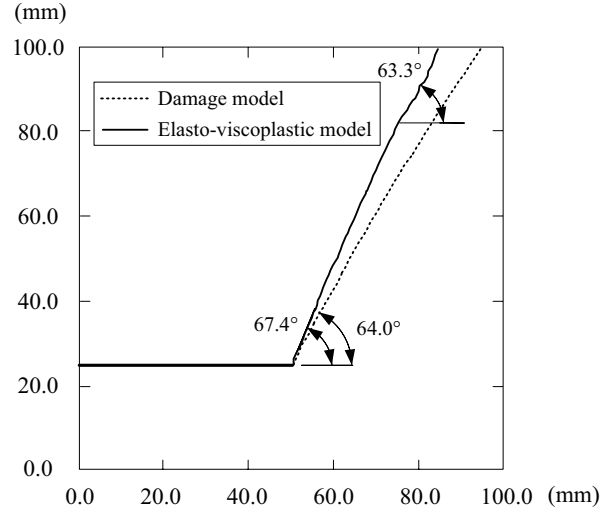


Figure 5.7. The crack paths of the simulations with the damage model and the elasto-viscoplastic model.

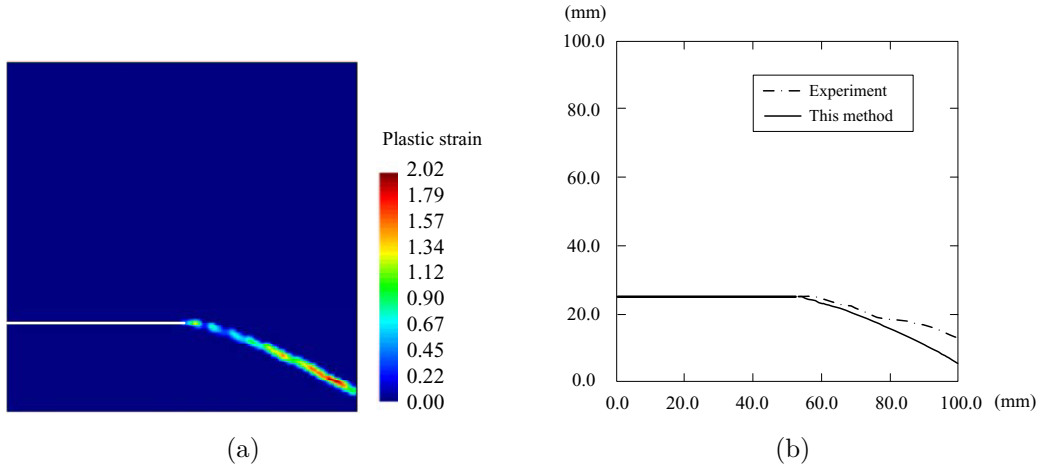


Figure 5.8. Dynamic shear band propagation: (a) effective plastic strain distribution at $t = 35.00 \mu\text{s}$ and (b) comparison of the computed shear band path with experimental results [56].

5.1.2. Crack branching

In this example, we consider a prenotched specimen 0.1 m *by* 0.04 m, as shown in Figure 5.9. Tensile tractions, $\sigma = 1 \text{ MPa}$, are applied on both the top and the bottom edges as a

step function in time. Numerical results for this problem have been given by Belytschko *et al.* [11], Rabczuk and Belytschko [61], Xu and Needleman [9] and experimental results with different dimensions are available in [62, 63, 64, 65, 66].

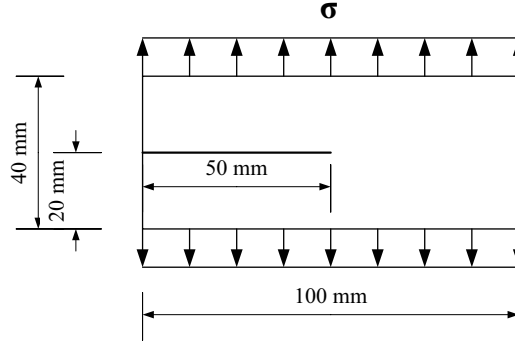


Figure 5.9. Plate with a horizontal initial notch under tensile loading.

We used the Lemaitre damage law [58] for the continuum domain and imposed a linear cohesive law with fracture cohesive energy $G_f = 3.0$ N/m once a discontinuity developed. The material properties are $\rho = 2450$ kg/m³, $E = 32$ GPa and $\nu = 0.20$. We used $A = 1.0$, $B = 7300.0$ and $\epsilon_{D_0} = 8.5 \times 10^{-5}$ for the Lemaitre damage model [58]. The initial Rayleigh wave speed is $c_R = 2119.0$ m/s. For the discretization, we modeled the domain with 50×21 , 100×51 , and 200×81 structured quadrilateral elements and used explicit time integration.

The crack branching phenomena is governed by the material stability criterion, which is a property of the constitutive equation. Crack branching was initiated when the two polarization angles from the material stability analysis differed from that of the previous crack direction. When this occurred, the crack was also injected into the adjacent elements. Unless the latter step was taken, crack branching could not be modeled accurately

with low order elements. For simplicity, we only allow the crack to branch once and set the element stress to zero in elements in which three cracks have formed.

The pattern of crack propagation is shown in Figure 5.10(a)-(c) along with a sketch of the experiment paths reported by Ramulu and Kobayashi [62]. The crack pattern is similar to the experimental results.

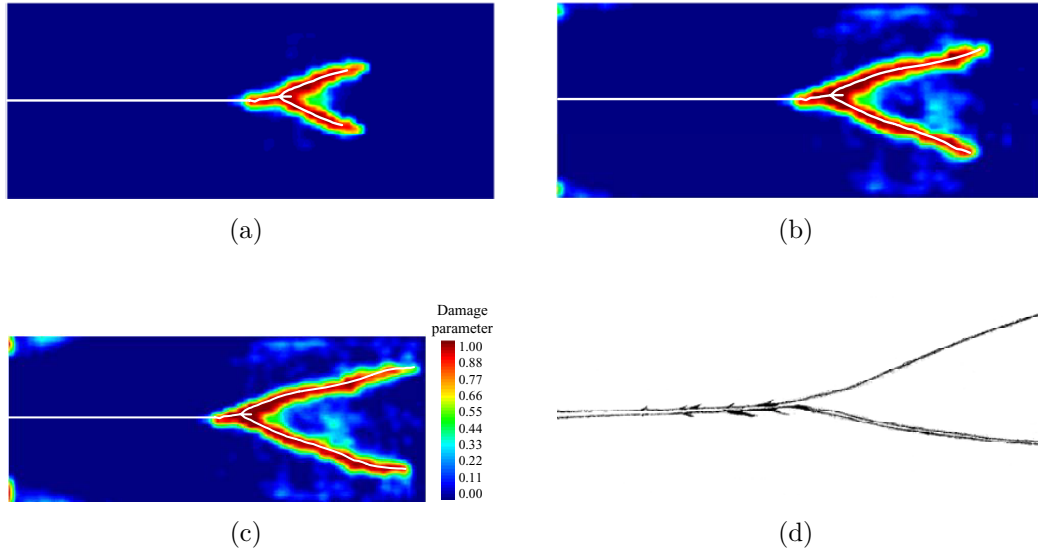


Figure 5.10. Crack branching and damage evolution with a 100×51 mesh at different time steps: (a) $t = 30.29 \mu s$ (b) $t = 46.14 \mu s$ (c) $t = 55.93 \mu s$ and (d) a sketch of the experiment paths reported by Ramulu and Kobayashi [62].

The computed crack propagation speed is shown in Figure 5.11(a) along with the reported crack propagation speed by Belytschko *et al.* [11]. The crack begins to propagate at $15.38 \mu s$. From this initial phase until crack branching, the crack tip speed increases linearly and peaks at around $29.04 \mu s$; at this point the crack branches into two cracks. After branching, the crack tip speed becomes almost constant at 75% of the Rayleigh wave speed. This agrees with the results which were reported by Belytschko *et al.* [11],

and Rabczuk and Belytschko [61]. The numerical simulation finishes at $55.93 \mu\text{s}$ when the crack tip reaches the boundary of the specimen.

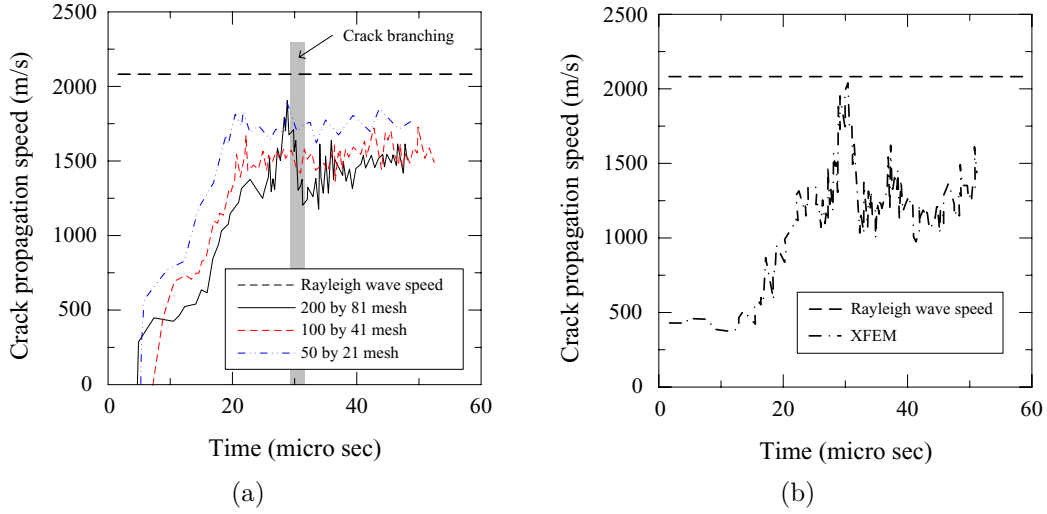


Figure 5.11. Crack propagation speed for the crack branching problem: (a) the current method and (b) the previous results in Reference [11].

5.1.2.1. Comparisons with the element deletion and the interelement crack methods. Figure 5.12 shows the results for the element deletion method at two different times. In these calculations, we used $G_f = 3 \text{ J/m}^2$ and $\epsilon_0 = 8.50 \times 10^{-5}$ for the linear elastic-linear softening law, where ϵ_0 is the strain at the peak stress. It can be seen

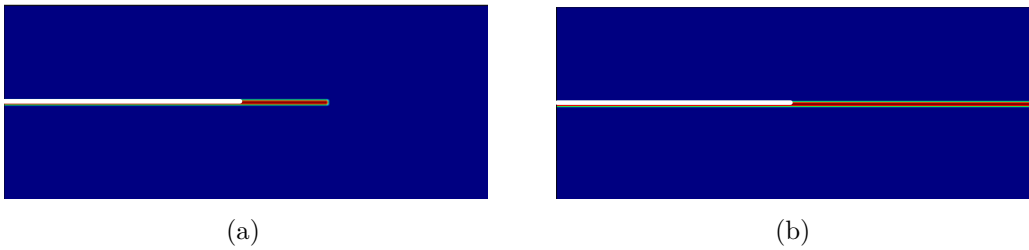


Figure 5.12. The final crack path of the element deletion method with a 200×81 structured quadrilateral mesh at different time steps: (a) $t = 30.56 \mu\text{s}$ and (b) $t = 65.62 \mu\text{s}$.

that the crack continues in a straight path without branching. The calculation shown was made with a 200×81 structured quadrilateral mesh, but we have also used 50×21 and 100×41 structured quadrilateral meshes and obtained a straight crack. One would expect the solution to exhibit an increase in the tensile strain adjacent to the crack as its velocity increases, which would trigger crack branching. In the simulation by the element deletion method, the stress adjacent to the crack tip does increase, but it never becomes large enough to initiate crack propagation in the lateral direction. The crack tip speeds

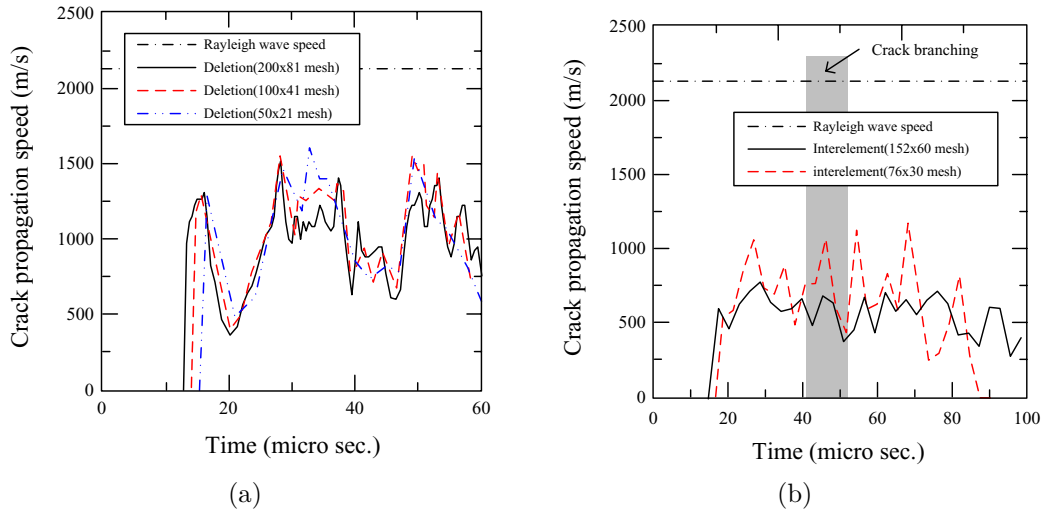


Figure 5.13. Crack propagation speed for the crack branching problem: (a) the element deletion method and (b) Camacho and Ortiz method [10].

for three different meshes computed by the element deletion method are shown in Figure 5.13(a). It can be seen that the crack tip velocity for all meshes is significantly less than that of XFEM. This is perhaps why branching does not occur. Also, the time history obtained by element deletion is completely different and bears little relationship to the results obtained by the other methods.

Figures 5.14(a)-(b) and (c)-(d) show the final paths obtained by Camacho and Ortiz method [10] for 76×30 and 152×60 structured cross-triangular meshes, respectively. In these calculations, $\sigma_c = 2.8$ MPa, $\delta_c = 3.9 \times 10^{-7}$ m and $\beta = 1.0$ were used for cohesive model [10]. The crack tip speeds for 76×30 and 152×60 structured cross-triangular meshes computed by the interelement crack method are shown in Figure 5.13(b). The interelement method predicts crack branching but the branching point depends somewhat on mesh refinement. Figure 5.15 shows the final crack paths for the element deletion

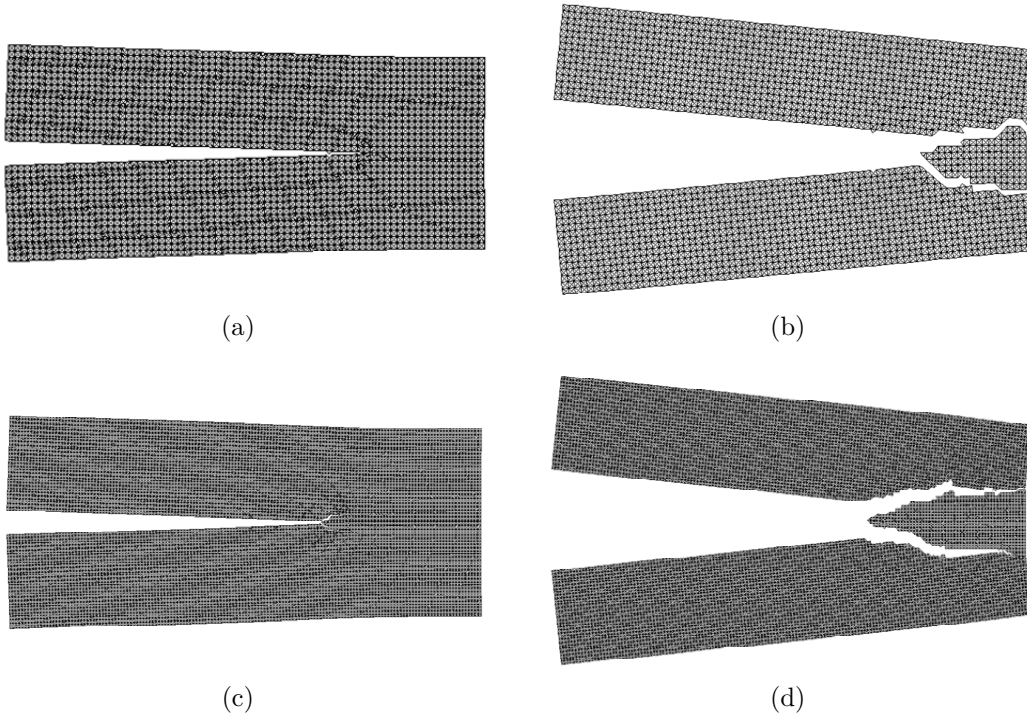


Figure 5.14. Crack path of the Camacho and Ortiz method [10] with: a 76×30 structured cross-triangular mesh at (a) $t = 48.38 \mu s$; (b) $t = 100.00 \mu s$ and a 152×60 structured cross-triangular mesh at (c) $t = 48.09 \mu s$; (d) $t = 100.0 \mu s$. The deformed shapes are magnified by 90.

method and for the interelement crack method with unstructured mesh. As we can see

from Figure 5.15(a), for an unstructured mesh, the element deletion method predicts crack branching, but it is quite different from the experimental observations [62].

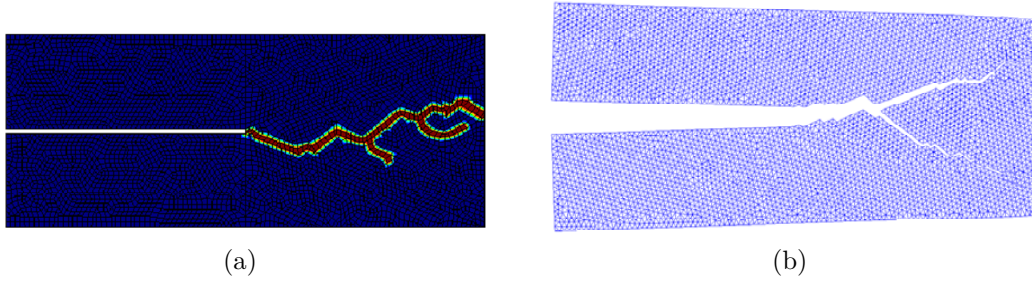


Figure 5.15. The final crack paths for unstructured meshes ($h_{avg}^e = 1.0$ mm): (a) the element deletion method and (b) the Camacho and Ortiz method [10]; the deformed shapes are magnified by 90.

We should make some remarks about the nucleation criteria in the interelement method and in XFEM. In the interelement method, the crack propagation was modeled strictly by separation of element edges. The only aspect of the algorithm that limits the evolution of the crack is the transition from edges that share nodes (and thus can not separate) to edges that have duplicated nodes (and thus can separate). In XFEM, the crack growth was governed by the material stability criterion, which is a property of the constitutive equation used. Crack branching was initiated when the two polarization angles from the material stability analysis differed from that of the previous crack direction. When this occurred, the crack was also injected into the adjacent elements. Unless the latter step was taken, crack branching could not be modeled accurately with XFEM with low order elements.

5.2. Dynamic fracture of thin shells

5.2.1. Notched cylinder fracture under internal detonation pressure

An interesting series of experiments concerned with the quasi-brittle fracture of shells has been reported by Chao and Shepherd [67], and Chao [68]. These experiments involve notched thin-wall pipes filled with gaseous explosives through which a detonation wave is passed. This is accomplished in the experiment by filling the pipe with an explosive gas and initiating a detonation wave at the left end as shown in Figure 5.16(a).

In this study, we focused on numerical simulations of two experimental results, *shot 7* ($L = 5.08$ cm) and *shot 4* ($L = 2.54$ cm) [67, 68], since these two experimental results exhibit strikingly different growth of the fracture, which is ascribed to the length of the notch. Chao and Shepherd [67], and Chao [68] reported that with a notch size of $L = 5.08$ cm, the *backward* crack tip, which is closer to the detonation initiation point, showed a curving crack path, whereas the *forward* crack tip propagates only a short distance in a straight line and then bifurcated into two cracks. However, with a notch size of $L = 2.54$ cm, the backward crack tip curved, whereas the forward crack tip propagates only a short distance in a straight line and then is arrested.

For the numerical simulation, we discretized the right segment of the cylinder length of the 91.40cm with 54,382 4-node quadrilateral shell elements ($h_e \simeq 0.90$ mm); see Figure 5.16(b)-(c). The shell material is aluminum 6061-T6 and we modeled it with J_2 -plasticity; the material properties are density $\rho = 2780.0$ kg/m³, Young's modulus $E = 69.0$ GPa, Poisson's ratio $\nu = 0.30$, and yield stress $\sigma_y = 275.0$ MPa. We used linear hardening with a constant slope $h_p = 640.0$ MPa. The cohesive fracture energy $G_f = 19.0$ kJ/m² is

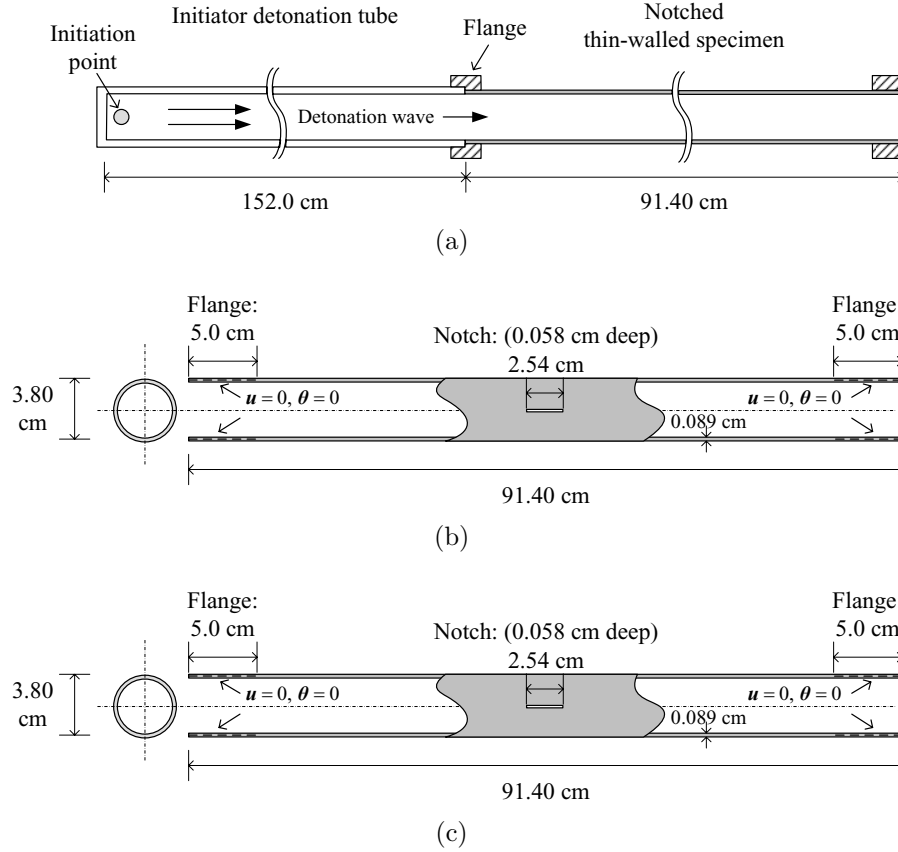


Figure 5.16. Setup for the notched cylinder fracture test under internal detonation pressure [67, 68]: (a) the total experiment assembly, (b) the cylinder with the notch size of $L = 5.08$ cm (*shot7*) and (c) the cylinder with a notch size of $L = 2.54$ cm (*shot4*).

treated in terms of a cohesive law (the assigned fracture energy is based on Johnson and Radon [69, 70] and Roychowdhury *et al.* [71]).

In order to induce unsymmetrical crack propagation with an axisymmetric shell structure and loading, we introduced a small scatter in the yield strength of the bulk material. The yield strength at every material points is perturbed by factors ranging from -5.0% to 5.0% : the perturbation factor is obtained from a log-normal distribution around the

mean value of 1.0 and a standard deviation of 2.0%. We also considered bulk materials in which the yield strength is perturbed by $\pm 10.0\%$; the results are almost identical.

For the fracture criterion, we used a 12% maximum tensile strain as the fracture strain. This strain value was used to nucleate any new cracks and to propagate cracks, but in these simulations no new cracks were nucleated as the notches and subsequent cracks served as the only nucleation mechanisms. The cracks were propagated in the direction normal to the direction of maximum principal strain.

For the applied pressure, we used a pressure time history function, $p(x, t)$, which is provided by Beltman and Shepherd [72]:

$$p(x, t) = \begin{cases} 0 & t < x/v^{cj} \\ p^{cj} \exp(-(t - x/v^{cj})/T_0) & t > x/v^{cj} \end{cases} \quad (5.1)$$

where x is the axial distance from the detonation initiation source to the material point, t is the simulation time, $T_0 (\simeq 3.0 \ x/v^{cj})$ is pressure decay time, and p^{cj} and v^{cj} are the Chapmand-Jouguet pressure and detonation wave propagation velocity, respectively. For the simulation, we used $p^{cj} = 6.2$ MPa and $v^{cj} = 2390$ m/s to model the internal detonation wave as in [72] and applied this pressure normal to all surfaces of the shell model throughout the entire simulation, even after extensive fracture and large deformation. Fluid-structure interaction effects were not modeled.

Here, we need to make a remark on the way we modeled the initial notch. The notches in the experiment were not machined through the entire depth of the shell. In this study, we modeled the notch by using the XFEM methodology, so we immediately allowed the translational and angular velocity fields across the notch to be discontinuous.

The penalty part of the cohesive law in the compressive regime was activated to prevent incompatibilities in the compressive part (below the notch), but the tensile part of the cohesive law is not activated in the notch since the fracture in the notch is assumed to be completed. The penalty constants for these constraints did not effect the final results very much.

5.2.1.1. Cylinder with notch size of $L = 5.08$ cm (shot 7). Figure 5.17 shows deformed configurations and contour plots of the effective plastic stress at the beginning of the backward crack propagation and just before and after the forward crack branches into two cracks. As we can see from Figure 5.17(c), the forward crack tip branches with an angle of 45° and forms stress concentrations ahead of the two branched tips. In contrast to the forward moving branched tips, the backward tip retains its straight path.

Figure 5.18 shows the different perspective views of the computed deformed configurations at an intermediate stage, time $t = 256.86 \mu s$. Subsequently, the forward branches turn to propagate along the circumferential direction. The computed final configuration is shown in Figure 5.19(a) along with the final experimental configuration, which is shown at Figure 5.19(b). The computation reproduces some of the key features of the experiment quite well. In the computations, the crack propagates from the notch to the backward and the forward tips. The forward propagating crack then branches initially at 45° , but then turns to propagate along the axis of the cylinder. The experimental specimen shows evidence of similar crack branching and turning. As can be seen from Figure 5.19(b), in the part of the pipe that has opened up, the crack progresses initially at an angle, but then the final crack path is circumferential, i.e. normal to the axis of the pipe. The computed

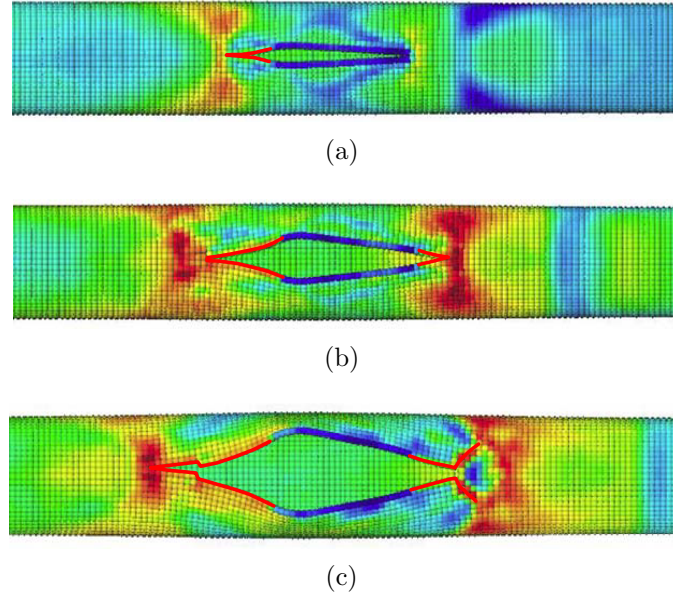


Figure 5.17. Evolution of the crack paths and the distributions of effective plastic stress for the cylinder with the notch size of $L = 5.08$ cm (*shot7*) at different time steps: (a) $t = 213.55 \mu\text{s}$, (b) $t = 228.61 \mu\text{s}$, and (c) $t = 238.01 \mu\text{s}$. Note that the finite element nodes are plotted and the crack paths are explicitly marked.

crack paths are quite similar. In the center of the fracture, a little wedge shaped pipe is apparent. This is absent in the computation.

There are some discrepancies in the final configurations as can be seen from Figure 5.19. The lower flap, as computed, opens up more than in the experiments. In the experiment, both the lower and the upper flaps show significant bends, but these are not apparent in the computation. This can be due to: (1) absence of fluid-structure interaction effects in the computation, (2) errors in detonation wave loading function, particularly in the later stages, and (3) lack of fidelity in fracture criterion or material model.

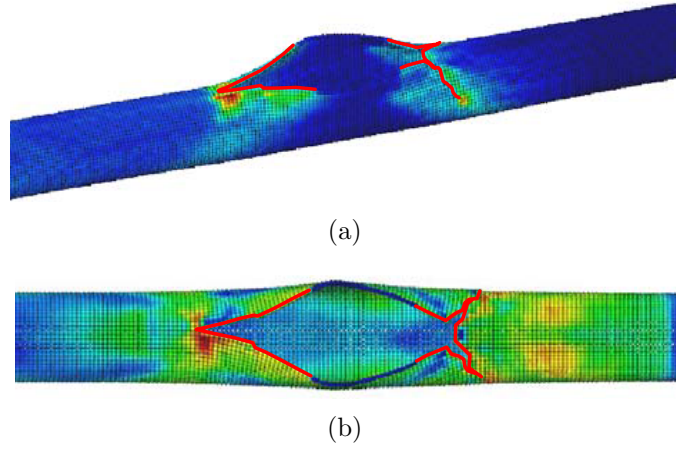


Figure 5.18. Crack opening at time $t = 256.86 \mu s$ along with the distribution of effective plastic stress for the cylinder with the notch size of $L = 5.08$ cm (*shot7*): (a) side view, and (b) top view. Note that the finite element nodes are plotted and the crack paths are explicitly marked.

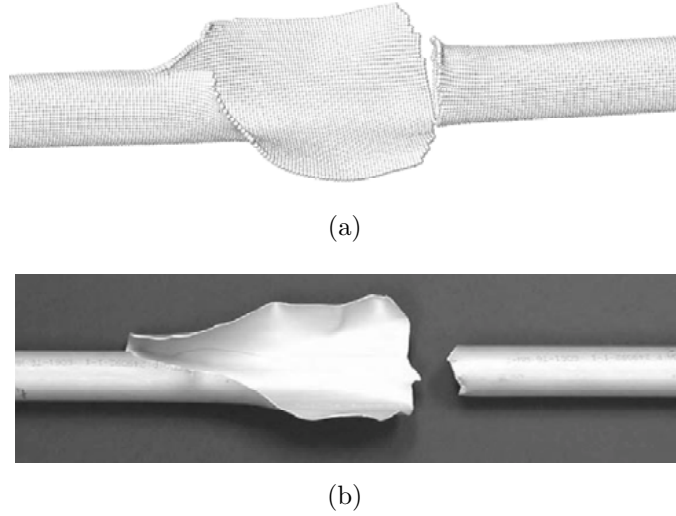


Figure 5.19. Comparison of the final deformed shape for the cylinder with the notch size of $L = 5.08$ cm (*shot7*): (a) the simulation result, and (b) the experimental result [67, 68].

Figure 5.20 shows time histories of the forward and backward crack propagation speeds. The forward crack tip starts to propagate around $t = 210.0 \mu s$ and then linearly speeds up and shows a peak speed around $t = 229.0 \mu s$; at this point the crack

branches into two cracks. After branching, the crack tip loses speed, but then the speed recovers and reaches a plateau.

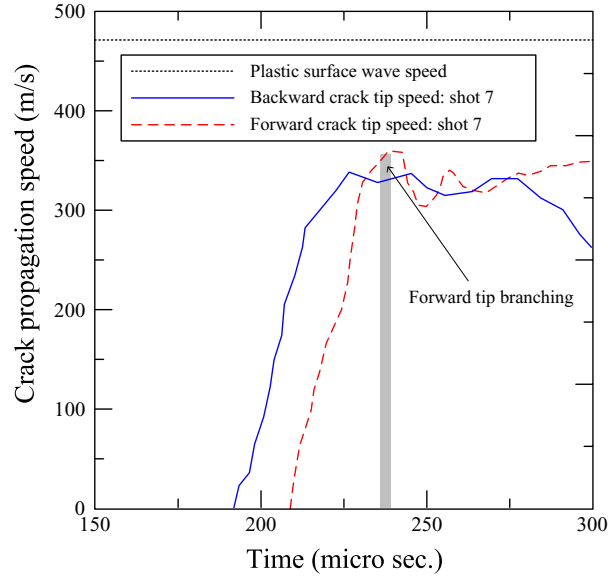


Figure 5.20. Propagation speeds of two crack tips for the cylinder with the notch size of $L = 5.08$ cm (*shot7*).

5.2.1.2. Cylinder with notch size of $L = 2.54$ cm (shot 4). Experiments with the shorter notch showed substantially different crack evolution, and this is also evident in the computations. Figure 5.21 shows the distribution of effective plastic stress in the computed deformed configuration before the backward crack starts to rotate. As can be seen from Figure 5.21(a), the axisymmetry of the stress field ahead of the backward crack tip is broken and then the crack tip path exhibits a change in direction as shown in Figure 5.21(b). Note that this sudden direction change of the crack path causes a concentration of plastic strain at the kinked points and it reduces the crack speed, as indicated in Figure 5.22.

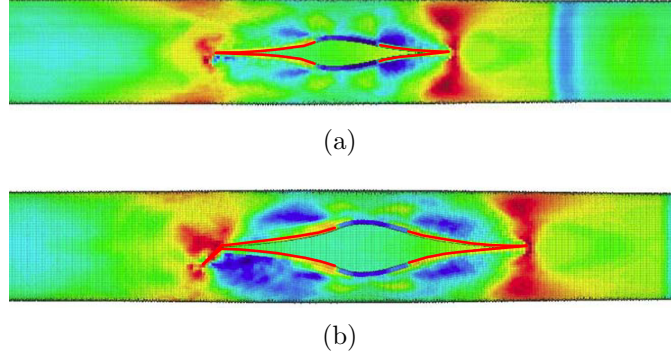


Figure 5.21. Evolution of the crack and the distributions of the effective plastic stress for the cylinder with the notch size of $L = 2.54$ cm (*shot4*) at different time steps: (a) $t = 231.41 \mu\text{s}$ and (b) $t = 239.05 \mu\text{s}$. Note that the finite element nodes are plotted and the crack paths are explicitly marked.

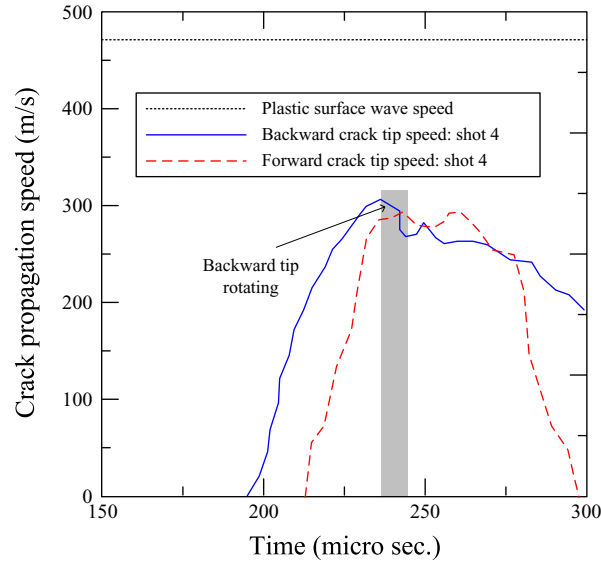


Figure 5.22. Crack propagation speeds of two crack tips for the cylinder with the notch size of $L = 2.54$ cm (*shot4*).

Figure 5.23 shows the different perspective views of the computed deformed configuration at time $t = 261.98 \mu\text{s}$. As we can see from the figure, the backward crack follows a circumferential path but the forward crack path remains straight. Shortly after this

point, the strain concentration ahead of forward crack tip is diffused and the crack tip is arrested.

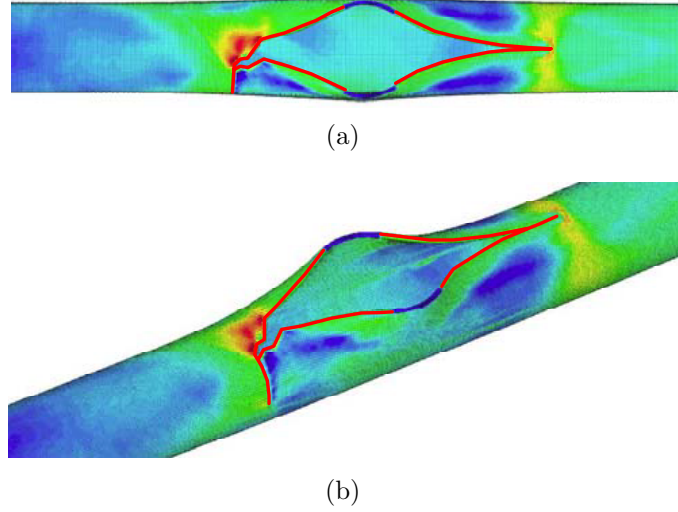


Figure 5.23. Evolution of the crack paths and the distributions of the effective plastic stress for the cylinder with the notch size of $L = 2.54$ cm (*shot4*) at time $t = 261.98 \mu\text{s}$: (a) top view and (b) side view. Note that the finite element nodes are plotted and the crack paths are explicitly marked.

A comparison between computational and experimental results of the final configuration is in Figure 5.24. Again, the computed size of the crack opening in the pipe agrees reasonably well with the experiment and so do the crack paths, except that the transition from the axial path to a circumferential path is quite smooth in the experiment, but rather rough in the computation. The shapes of the flaps are not predicted well. Evidently, fluid-structure interaction effects play a substantial role in their shapes.

The computed crack propagation speeds for *shot 7* and *shot 4*, which are shown in Figures 5.20 and 5.22, respectively, are somewhat faster than the reported experimental crack

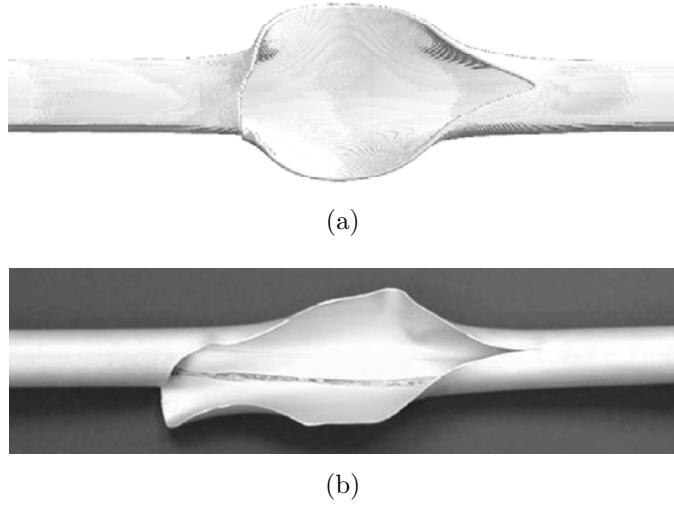


Figure 5.24. Comparison of the final deformed shape for the cylinder with the notch size of $L = 2.54$ cm (*shot4*) at time $t = 298.1 \mu\text{s}$: (a) the simulation result, and (b) the experimental result (*shot 4*).

speeds (maximum 250 m/s) [68]. This may be due to the shortcomings in the numerical representation of the crack: i.e. lack of crack tip blunting and tunneling phenomena.

CHAPTER 6

Conclusions

Finite element methods which are incorporated within an explicit time integration scheme have been developed for the prediction of dynamic fracture in shells and dynamic crack and shear band propagation in two dimensional planes. In the methods, by reinterpreting the conventional XFEM displacement field, a cracked or sheared element is represented by two superposed elements with a set of added phantom nodes or phantom degrees of freedom. The numerical integration of those elements is simplified by the use of an one point quadrature scheme with a hourglass control. This facilitates the implementation of the methods into standard finite element programs. Another attractive feature of the methods is that they provides consistent history variables and low computational cost. This allows large scale nonlinear dynamic fracture problems to be solved efficiently.

A nonlocal fracture criterion based on the maximum tensile principal strain has been developed for the modeling dynamic fracture in a quasi-brittle material. In order to mitigate spurious predictions of fracture within the framework of an explicit time integration scheme, the criterion uses a weighted average of the strain ahead of the crack tip, i.e. a nonlocal form of a strain-based fracture criterion. For the weighting function, a cubic spline that extends to approximately the edge of the near tip plastic field was used. For the modeling of shear band propagation in a rate-dependent material, the material stability criterion also used.

Fracture energy dissipation was modeled by a cohesive law across the crack and shear band surfaces. The cohesive law serves to represent plastic work and other fracture processes that are not resolved by the model.

To evaluate the applicability of the proposed method, several numerical examples for which experimental or numerical results are available have been analyzed for two dimensional plane and shell fracture problems. In the Kalthoff and Winkler [54] problem, which is handled with two dimensional elements, the method showed a little mesh dependency: the crack tip speed decreases somewhat with mesh size. We attribute this effect to the elementwise cracking procedure, i.e. due to the absence of a model for a partially cracked element. It is apparent that the elementwise cracking approach requires finer meshes to match the accuracy of methods with partial element cracking. So while the elementwise progression of a crack is simple, it tends to overestimate the crack speed. However, overall crack and shear band propagation paths are in reasonable agreement with what was obtained experimentally. In the dynamic crack branching problem, we found that the proposed method is quite effective for these complicated crack patterns.

Simulations of shell fracture were made for two of the Chao and Shepherd [67] experiments of explosively loaded pipes. The finite element model was directly loaded by the pressure time history of the detonation traveling wave; fluid-structure interaction effects were not considered. Nevertheless, the computations reproduce many of the salient features of each experiment and the differences in the crack paths between two experiments. For the pipe with the longer pre-notch, the computations correctly predict crack branching at one end and the subsequent wrap-around of the crack path that severs the pipe at the other end. For the pipe with a shorter pre-notch, a twisting of the crack path is

correctly predicted. However, the deformed configurations observed experimentally shows some deformations of the flaps of the pipe that are not replicated by the computation. These are probably due to fluid-structure interaction effects that were not modeled.

Overall, these computational results show substantial promise for predicting the dynamic fracture behavior of two dimensional plane and shell structures. They furthermore indicate that the methods lend a great support for the simulations of dynamic fracture involving nonlinearities.

References

- [1] T. Belytschko and T. Black. Elastic crack growth in finite elements with minimal remeshing. *International Journal for Numerical Methods in Engineering*, 45(5):601–620, 1999.
- [2] N. Moës, J. Dolbow, and T. Belytschko. A finite element method for crack growth without remeshing. *International Journal for Numerical Methods in Engineering*, 46(1):131–150, 1999.
- [3] A. R. Ingraffea, W. Gerstle, P. Gergely, and V. Saouma. Fracture mechanics in bond reinforced concrete. *Journal of Structural Division*, ASCE, 110(4):871–890, 1984.
- [4] D. V. Swenson and A. R. Ingraffea. A finite element model of dynamic crack propagation with an application to intersecting cracks. In A. R. Luxmoore, D. R. J. Owen, Y. P. S. Rajapakse, and M. F. Kanninen, editors, *IV International Conference on Numerical Methods in Fracture Mechanics*, Texas, U.S.A., 1987.
- [5] D. V. Swenson and A. R. Ingraffea. Modelling mixed-mode dynamic crack propagation using finite elements: theory and applications. *Computational Mechanics*, 3:187–192, 1988.
- [6] T. Bittencourt, A. Ingraffea, and J. Llorca. Simulation of arbitrary, cohesive crack propagation. In Z. P. Bažant, editor, *Fracture mechanics of concrete structures*, pages 339–350, 1992.
- [7] L.F. Martha, P.A. Wawrzynek, and A.R. Ingraffea. Arbitrary crack representation using solid modeling. *Engineering with Computers*, 9:63–82, 1993.
- [8] J.B.C. Neto, P.A. Wawrzynek, M.T.M. Carvalho, L.F. Martha¹, and A.R. Ingraffea. An algorithm for three-dimensional mesh generation for arbitrary regions with cracks. *Engineering with Computers*, 17:75–91, 2001.
- [9] X.-P. Xu and A. Needleman. Numerical simulation of fast crack growth in brittle solids. *Journal of the Mechanics & Physics of Solids*, 42(9):1397–1434, 1994.

- [10] G. Camacho and M. Ortiz. Computational modelling of impact damage in brittle materials. *International Journal of Solids and Structures*, 33:2899–2938, 1996.
- [11] T. Belytschko, H. Chen, J. Xu, and G. Zi. Dynamic crack propagation based on loss of hyperbolicity with a new discontinuous enrichment. *International Journal for Numerical Methods in Engineering*, 58:1873–1905, 2003.
- [12] G. Zi, J. H. Song, S. H. Lee E. Budyn, and T. Belytschko. A new method for multiple cracks and its application to fatigue crack growth. *Modeling and Simulations in Materials Science and Engineering*, 12:901–915, 2004.
- [13] E. Budyn, G. Zi, N. Moës, and T. Belytschko. A method for multiple crack growth in brittle materials without remeshing. *International Journal for Numerical Methods in Engineering*, 61:1741–1770, 2004.
- [14] J. H. Song, P. M. A. Areias, and T. Belytschko. A method for dynamic crack and shear band propagation with phantom nodes. *International Journal for Numerical Methods in Engineering*, 67:868–893, 2006.
- [15] P. M. A. Areias and T. Belytschko. Analysis of three-dimensional crack initiation and propagation using the extended finite element method. *International Journal for Numerical Methods in Engineering*, 63:760–788, 2005.
- [16] P. M. A. Areias, J. H. Song, and T. Belytschko. A finite-strain quadrilateral shell element based on discrete Kirchhoff-Love constraints. *International Journal for Numerical Methods in Engineering*, 64:1166–1206, 2005.
- [17] P. M. A. Areias, J. H. Song, and T. Belytschko. Analysis of fracture in thin shells by overlapping paired elements. *Computer Methods in Applied Mechanics and Engineering*, 195:5343–5360, 2006.
- [18] J. H. Song and T. Belytschko. Dynamic fracture of shells subjected to impulsive loads. *Journal of Applied Mechanics*, in review, 2008.
- [19] J. M. Melenk and I. Babuška. The partition of unity finite element method: Basic theory and application. *Computer Methods in Applied Mechanics and Engineering*, 39:289–314, 1996.
- [20] I. Babuška and J. M. Melenk. The partition of unity method. *International Journal for Numerical Methods in Engineering*, 40(4):727–758, 1997.

- [21] M. Stolarska, D. L. Chopp, N. Moës, and T. Belytschko. Modeling crack growth by level sets in the extended finite element method. *International Journal for Numerical Methods in Engineering*, 51(8):943–960, 2001.
- [22] T. Belytschko, N. Moës, S. Usui, and C. Parimi. Arbitrary discontinuities in finite elements. *International Journal for Numerical Methods in Engineering*, 50(4):993–1013, 2001.
- [23] G. Ventura, J. X. Xu, and T. Belytschko. A vector level set method and new discontinuity approximations for crack growth by EFG. *International Journal for Numerical Methods in Engineering*, 54:923–944, 2002.
- [24] G. Ventura, E. Budyn, and T. Belytschko. Vector level sets for description of propagating cracks in finite elements. *International Journal for Numerical Methods in Engineering*, 58:1571–1592, 2003.
- [25] B. Prabel, A. Combescure, A. Gravouil, and S. Marie. Level set X-FEM non-matching meshes: application to dynamic crack propagation in elastic-plastic media. *International Journal for Numerical Methods in Engineering*, 69:1553–1569, 2007.
- [26] J. H. Song, H.W. Wang, and T. Belytschko. A comparative study on finite element methods for dynamic fracture. *Computational Mechanics*, DOI 10.1007/s00466-007-0210-x.
- [27] M. Ortiz and A. Pandolfi. Finite-deformation irreversible cohesive elements for three-dimensional crack-propagation analysis. *International Journal for Numerical Methods in Engineering*, 44:1267–1282, 1999.
- [28] K. D. Papoulia, C. H. Sam, and S. A. Vavasis. Time continuity in cohesive finite element modeling. *International Journal for Numerical Methods in Engineering*, 58:679–701, 2003.
- [29] K. D. Papoulia, S. A. Vavasis, and P. Ganguly. Spatial convergence of crack nucleation using a cohesive finite-element model on a pinwheel-based mesh. *International Journal for Numerical Methods in Engineering*, 67:1–16, 2006.
- [30] F. Zhou and J. F. Molinari. Dynamic crack propagation with cohesive elements: a methodology to address mesh dependency. *International Journal for Numerical Methods in Engineering*, 59:1–24, 2004.
- [31] A. Hansbo and P. Hansbo. A finite element method for the simulation of strong and weak discontinuities in solid mechanics. *Computer Methods in Applied Mechanics and Engineering*, 193:3523–3540, 2004.

- [32] P. M. A. Areias and T. Belytschko. A comment on the article: A finite element method for simulation of strong and weak discontinuities in solid mechanics. *Computer Methods in Applied Mechanics and Engineering*, 195:1275–1276, 2006.
- [33] T. Belytschko, W. K. Liu, and B. Moran. *Nonlinear finite elements for continua and structures*. John Wiley & Sons Ltd., New York, 2000.
- [34] D. P. Flanagan and T. Belytschko. A uniform strain hexahedron and quadrilateral with orthogonal hourglass control. *International Journal for Numerical Methods in Engineering*, 17:679–706, 1981.
- [35] W. J. T. Daniel and T. Belytschko. Suppression of spurious intermediate frequency modes in under-integrated elements by combined stiffness/viscous stabilization. *International Journal for Numerical Methods in Engineering*, 64:335–353, 2005.
- [36] J. Réthoré, A. Gravouil, and A. Combescure. An energy-conserving scheme for dynamic crack growth using the extended finite element method. *International Journal for Numerical Methods in Engineering*, 63:631–659, 2005.
- [37] T. Elguedj, A. Gravouil, and A. Combescure. Appropriate extended functions for x-fem simulation of plastic fracture mechanics. *Computer Methods in Applied Mechanics and Engineering*, 195:501–515, 2006.
- [38] F. Cirak, M. Ortiz, and A. Pandolfi. A cohesive approach to thin-shell fracture and fragmentation. *Computer Methods in Applied Mechanics and Engineering*, 194:2604–2618, 2005.
- [39] P. M. A. Areias and T. Belytschko. Nonlinear analysis of shells with arbitrary evolving cracks using XFEM. *International Journal for Numerical Methods in Engineering*, 62:384–415, 2005.
- [40] S. Ahmad, B. B. Irons, and O. C. Zienkiewicz. Analysis of thick and thin shell structures by curved finite elements. *International Journal for Numerical Methods in Engineering*, 2:419–451, 1970.
- [41] T. J. R. Hughes and W. K. Liu. Nonlinear finite element analysis of shells: Part 1, Two dimensional shells. *Computer Methods in Applied Mechanics and Engineering*, 26:167–181, 1981.
- [42] T. J. R. Hughes and W. K. Liu. Nonlinear finite element analysis of shells: Part 2, Three dimensional shells. *Computer Methods in Applied Mechanics and Engineering*, 26:331–362, 1981.

- [43] T. Belytschko, J. I. Lin, and C. S. Tsay. Explicit algorithms for the nonlinear dynamics of shells. *Computer Methods in Applied Mechanics and Engineering*, 42:225–251, 1984.
- [44] T. Belytschko, B. L. Wong, and H. Y. Chiang. Advances in one-point quadrature shell elements. *Computer Methods in Applied Mechanics and Engineering*, 96:93–107, 1992.
- [45] T. Belytschko and W. E. Bachrach. Efficient implementation of quadrilaterals with high coarse-mesh accuracy. *Computer Methods in Applied Mechanics and Engineering*, 54:279–301, 1986.
- [46] T. Belytschko and I. Leviathan. Physical stabilization of the 4-node shell element with one point quadrature. *Computer Methods in Applied Mechanics and Engineering*, 113:321–350, 1994.
- [47] T. Rabczuk, J. H. Song, and T. Belytschko. Cracking particles method: simulations of instability in dynamic fracture. *Engineering Fracture Mechanics*, in review.
- [48] J. Lemaitre and J. L. Chaboche. *Mechanics of Solid Materials*. Cambridge University Press, Cambridge, 1990.
- [49] P. Perzyna. *Thermodynamic theory of viscoplasticity*. Academic Press, New York, 1971.
- [50] J. Lemonds and A. Needleman. Finite element analyses of shear localization in rate and temperature dependent solids. *Mechanics of Materials*, 5:339–361, 1986.
- [51] M. Zhou, G. Ravichandran, and A. J. Rosakis. Dynamically propagating shear bands in impact-loaded prenotched plates-ii. numerical simulations. *Journal of the Mechanics & Physics of Solids*, 44:1007–1032, 1996.
- [52] S. Li, W. K. Liu, A. J. Rosakis, T. Belytschko, and W. Hao. Meshfree Galerkin simulations of dynamic shear band propagation and failure mode transition. *International Journal of Solids and Structures*, 39:1213–1240, 2002.
- [53] D. Peirce, C. F. Shih, and A. Needleman. A tangent modulus method for rate dependent solids. *Computers & Structures*, 18:875–887, 1984.
- [54] J. F. Kalthoff and S. Winkler. Failure mode transition at high rates of shear loading. *International Conference on Impact Loading and Dynamic Behavior of Materials*, 1:185–195, 1987.

- [55] Y. J. Lee and L. B. Freund. Fracture initiation due to asymmetric impact loading of an edge cracked plate. *Journal of Applied Mechanics*, ASME, 57:104–111, 1990.
- [56] J. F. Kalthoff. Modes of dynamic shear failure in solids. *International Journal of Fracture*, 101:1–31, 2000.
- [57] R. F. Decker. *Source Book on Maraging Steels*. American Society for Metals, 1979.
- [58] J. Lemaitre. Evaluation of dissipation and damage in metal submitted to dynamic loading. In *Proceedings ICM 1*, 1971.
- [59] T. Belytschko, Y. Y. Lu, L. GU, and M. Tabbara. Element-free Galerkin methods for static and dynamic fracture. *International Journal for Numerical Methods in Engineering*, 32:2547–2570, 1995.
- [60] T. Belytschko and M. Tabbara. Dynamic fracture using element-free Galerkin methods. *International Journal for Numerical Methods in Engineering*, 39:923–938, 1996.
- [61] T. Rabczuk and T. Belytschko. Cracking particles: a simplified meshfree method for arbitray evolving cracks. *International Journal for Numerical Methods in Engineering*, 61:2316–2343, 2004.
- [62] M. Ramulu and A. S. Kobayashi. Mechanics of crack curving and branching—a dynamic fracture analysis. *International Journal of Fracture*, 27:187–201, 1985.
- [63] K. Ravi-Chandar. Dynamic fracture of nominally brittle materials. *International Journal of Fracture*, 90:83–102, 1998.
- [64] E. Sharon, S. P. Gross, and J. Fineberg. Local crack branching as a mechanism for instability in dynamic fracture. *Physical Review Letter*, 74(25):5096–5099, 1995.
- [65] E. Sharon and J. Fineberg. Microbranching instability and the dynamic fracture of brittle materials. *Physical Review B*, 54(10):7128–7139, 1996.
- [66] J. Fineberg, E. Sharon, and G. Cohen. Crack front waves in dynamic fracture. *International Journal of Fracture*, 119:247–261, 2003.
- [67] T. W. Chao and J. E. Shepherd. Fracture response of externally-flawed cylindrical shells to internal gaseous detonation loading. In *Emerging technologies in Fluids, Structures, and Fluid/Structure Interactions*, pages 85–98, ASME Pressure Vessels and Piping Conference, Vancouver, BC, 2002.

- [68] T. W. Chao. *Gaseous detonation-driven fracture of tubes*. PhD thesis, California Institute of Technology, U.S.A., 2004.
- [69] F. A. Johnson and J. C. Radon. Evaluation of fracture energy of aluminum alloys. *Journal of Testing and Evaluation*, 3:364–367, 1975.
- [70] F. A. Johnson and J. C. Radon. Fracture energy and crack tunnelling. *Journal of Testing and Evaluation*, 4:209–217, 1976.
- [71] S. Roychowdhury, Y. D. A. Roy, and R. H. Dodds Jr. Ductile tearing in thin aluminum panels: experiments and analyses using large-displacement, 3-D surface cohesive elements. *Engineering Fracture Mechanics*, 69:983–1002, 2002.
- [72] W. M. Beltman and J. E. Shepherd. Linear elastic response of tubes to internal detonation loading. *Journal of Sound and Vibration*, 252:617–655, 2002.

Vita

Name: Jeong-Hoon Song

Place of Birth: Seoul, Republic of Korea

Education:

2004.08-2008.06, Ph.D., Theoretical and Applied Mechanics, Northwestern University, U.S.A.

2001.03-2003.02, M.S., Department of Civil Engineering, Yonsei University, Korea

1997.03-2001.02, B.S., School of Civil & Urban Engineering, Yonsei University, Korea

Professional Research Experiences:

2004.02-2004.07, Associate Researcher, Disaster Research Center, Yonsei University, Korea

2003.03-2004.01, Pre-doctoral fellow, Northwestern University, U.S.A.

Selected Publications:

Refereed Journal Articles & Chapters in Books

1. J.H. Song and T. Belytschko. Dynamic Fracture of Shells Subjected to Impulsive Loads, *Journal of Applied Mechanics*, in review.
2. T. Rabczuk, J.H. Song and T. Belytschko. Cracking Particles Method: Simulations of Instability in Dynamic Fracture, *Engineering Fracture Mechanics*, accepted.
3. J.H. Song, H.W. Wang and T. Belytschko. A comparative study on finite element methods for dynamic fracture, *Computational Mechanics*, DOI 10.1007/s00466-007-0210-x, in early view.

4. T. Belytschko, S. Loehnert and J.H. Song. Multiscale aggregating discontinuities: A method for circumventing loss of material stability, *International Journal for Numerical Methods in Engineering*, **73**: 869–894, 2008.
5. T. Belytschko, J.H. Song, H.W. Wang and R. Gracie. *On applications of XFEM to dynamic fracture and dislocations*, IUTAM Symposium on Discretization Methods for Evolving Discontinuities, edited by A. Combescure, R. de Borst and T. Belytschko, Springer, 2007.
6. J.H. Song, P.M.A. Areias and T. Belytschko. A method for dynamic crack and shear band propagation with phantom nodes, *International Journal for Numerical Methods in Engineering*, **67**: 868-893, 2006.
7. P.M.A. Areias, J.H. Song and T. Belytschko. Analysis of fracture in thin shells by overlapping paired elements, *Computer Methods in Applied Mechanics and Engineering*, **195**: 5343-5360, 2006.
8. P.M.A. Areias, J.H. Song and T. Belytschko. A finite-strain quadrilateral shell element based on discrete Kirchhoff-Love constraints, *International Journal for Numerical Methods in Engineering*, **64**: 1166-1206, 2005.
9. G. Zi, J.H. Song, E. Budyn, S.H. Lee and T. Belytschko. A new method for multiple cracks and its application to fatigue crack growth, *Modeling and Simulations in Materials Science and Engineering*, **12**: 901-915, 2004.
10. S.H. Lee, J.H. Song, Y.C. Yoon, G. Zi and T. Belytschko. Combined extended and superimposed finite element method for crack, *International Journal for Numerical Methods in Engineering*, **59**: 1119-1136, 2004.